

THESIS

STRESSES AND FREQUENCY SHIFTS IN FULLY EXTENDED AND FOLDED WIND  
TURBINE BLADES

Submitted by

Wael Abdalrwaf

Department of Civil and Environmental Engineering

In partial fulfillment of the requirements

For the Degree of Master of Science

Colorado State University

Fort Collins, Colorado

Fall 2017

Master's Committee:

Advisor: Paul Heyliger

Donald Radford  
Rebecca Atadero

Copyright by Wael Abdalrwaf 2017

All Rights Reserved

## ABSTRACT

### STRESSES AND FREQUENCY SHIFTS IN FULLY EXTENDED AND FOLDED WIND TURBINE BLADES

Alternative methods for generating energy have grown in the application in the past few decades. The main objective of this research is to understand the changes in the displacements, stresses, and natural frequencies of fully extended and folded wind turbine blades. A comparative study of the folded blade of fitted properties with the fully extended wind turbine blade was achieved. Folded blades could be more efficient in generating electricity from the wind for turbines with small radii and could be beneficial for transportation purposes.

In this study, a basic model of fully extended and folded blades was completed using three-dimensional linear elasticity model and the finite element method. Two different load cases were analyzed to study the conventional and folded blade behaviors. By using the wind load alone, an initial analysis is achieved as the wind load is applied to observe the blade behavior under standard conditions. For more practical consideration, both wind and gravity load were then applied. The study estimates the changes in stresses, displacements, and natural frequencies when the blades are folded and helps better understanding the necessary design parameters of these structures. Finally, free vibration behavior of the folded and extended blades is considered.

## ACKNOWLEDGMENTS

I would like to express my gratitude to my advisor; Dr. Paul Heyliger, for his continuous support of my research. I am indebted to the patience, enthusiasm and knowledge that he bestowed upon me. My sincere thanks also go to the additional members of my committee: Dr. Donald Radford and Dr. Rebecca Atadero. Thank you for supporting my research and the interest that you have given to my education and the progression of this research project.

I would personally like to thank my family for their faith, prayers, and the daily support that they have given me. To my parents who inspire me daily, my sisters who encourages me with such a fierce passion, and to my brothers for their calm demeanor in assisting me through all aspects of this research. I am forever grateful. Also, for my best friends for the encouragement and the support for the long journey.

Finally, I offer this project to my God (Allah) without whom my life would not have meaning or purpose.

## TABLE OF CONTENTS

ABSTRACT.....	ii
ACKNOWLEDGMENTS .....	iii
LIST OF TABLES .....	vi
LIST OF FIGURES .....	vii
INTRODUCTION .....	1
LITERATURE REVIEW .....	6
THE METHODOLOGY.....	15
3.1.  Governing Equations.....	15
3.2.  Blade Material and Geometry: .....	24
3.2.1.  The Box Spar Details .....	26
3.2.2.  The Skin Details.....	26
3.3.  The Folded Blade Details.....	27
3.4.  Finite Element Model.....	27
ANALYSIS.....	30
4.1.  Static Deflection Calculations.....	30
4.1.1.  Wind Load (Live Loading) .....	30
4.1.2.  Gravity Load (Dead Load).....	31
4.2.  Deflections Calculations .....	33
4.3.  Stresses Calculations .....	34

4.4.	Frequency and Model Shape Calculations .....	34
RESULTS .....		35
5.1.	Dead Load Case .....	35
5.1.1.	Static Deflection for the Blade.....	35
5.1.2.	Stresses in the Blade Skin.....	36
5.1.3.	Stresses in the Box Spar.....	38
5.2.	Live plus Dead Load Case (Wind + Gravity) .....	41
5.2.1.	Static Deflection for the Blade.....	41
5.2.2.	Stresses at the Skin.....	41
5.2.3.	Stresses in the Box .....	44
5.3.	Stress as a Function of Position.....	46
5.3.1.	Fully Extended Blade.....	46
5.3.2.	The Folded Blade.....	49
5.4.	Folded Blade Stresses at The Cutting Edges:.....	52
5.5.	Fundamental Frequency of Vibration .....	54
5.5.1.	Vibrational Mode and Frequency of Blade.....	54
DISCUSSION .....		57
6.1.	Static Deflection:.....	57
6.2.	Stresses:.....	58
CONCLUSIONS.....		63
REFERENCES .....		65

## LIST OF TABLES

Table 3.1: Material Properties of Poly-Carbon Fiber and Glass Fiber for Blade Modeling (Performance Composites, 2014). .....	28
Table 5.1: Vibrational Modes and Frequencies of Conventional Blades. ....	54
Table 5.2: Vibrational Modes and Frequencies of Folded Blades. ....	54

## LIST OF FIGURES

Figure 1.1: Energy efficiency areas and folded blade (Xie et al. 2015). .....	2
Figure 1.2: Three-dimensional sketches of conventional and folded wind turbine blade. ....	3
Figure 1.3: The conventional turbine blade. ....	4
Figure 2.1: A 75 meter Siemens blade being driven over a roundabout berm in Denmark in August 2012 (Danish Television). ....	11
Figure 2.2: A 30-ton blade transported on the road across Funen and Jutland in Denmark, July 2013 (Danish Television). ....	11
Figure 2.3: Schematic diagram of the folded blade (Xie et al. 2015). ....	12
Figure 2.4: Cross-sectional details of a wind turbine blade (Stackpole, 2011). ....	14
Figure 3.1: The NREL's S818 Airfoil. ....	25
Figure 3.2: The blade planform profile. ....	25
Figure 3.3: The connection between the skin and the box spar. ....	28
Figure 3.4: The folded blade. ....	29
Figure 3.5: Axes of the blade model. ....	29
Figure 4.1: Fully extended and folded blade under both load cases. ....	32
Figure 4.2: Fully extended blade under both load cases while rotating. ....	32
Figure 4.3: Folded blade under both load cases while rotating. ....	33
Figure 4.4: Coordinates of the nodes selected for static displacements. ....	34
Figure 5.1: Static deflection for the fully extended blade. ....	35
Figure 5.2: The deflected and the von Mises contour for the fully extended blade. ....	36
Figure 5.3: The von Mises stresses for the fully extended blade. ....	36

Figure 5.4: Compression stresses in the z-direction for the fully extended blade surface.....	37
Figure 5.5: Tensile stress in the z-direction for the fully extended blade surface. ....	37
Figure 5.6: The stresses contour for ( $\sigma_{zz}$ ) for the fully extended blade. ....	38
Figure 5.7: The von Mises stress on the tensile and compressive faces of the box spar. ....	38
Figure 5.8: The deflection and von Mises contours for the box spar. ....	39
Figure 5.9: Compressive stresses in the z-direction for the box spar surface.....	39
Figure 5.10: Tensile stresses in the z-direction for the box spar surface.....	40
Figure 5.11: Stresses contours for ( $\sigma_{zz}$ ) for the full box spar.....	40
Figure 5.12: Static deflection for the fully extended blade.....	41
Figure 5.13: The deflection and von Mises stress contour for the conventional blade. ....	42
Figure 5.14: The differences of the von Mises stress in two surfaces for the fully extended blade. .....	42
Figure 5.15: Compressive bending stresses in the z-direction.....	43
Figure 5.16: Tensile bending stresses in the z-direction.....	43
Figure 5.17: The stresses contours for ( $\sigma_{zz}$ ) for the fully extended blade.....	43
Figure 5.18: The differences of the von Mises stress in two surfaces for box spar.....	44
Figure 5.19: The deflection and von Mises stress contour for the box spar. ....	44
Figure 5.20: Compressive stresses in the z-direction.....	45
Figure 5.21: Tensile stresses in the z-direction.....	45
Figure 5.22: Stresses contour for ( $\sigma_{zz}$ ) for the full box spar. ....	46
Figure 5.23: The von Mises stress while the blade rotation. ....	47
Figure 5.24: The principle stresses ( $\sigma_{zz}$ ) in z-direction while the blade rotation.....	47

Figure 5.25: Stresses ( $\sigma_{zz}$ ) contour while the blade rotated at $0^\circ$ , $90^\circ$ , and $180^\circ$ . The position of the blade is changed for viewing purposes. ....	48
Figure 5.26: The von Mises stresses while the blade rotation. ....	50
Figure 5.27: The principle stresses ( $\sigma_{zz}$ ) in z-direction while the blade rotation. ....	50
Figure 5.28: The comparison in von Mises stresses between conventional and folded blade. ....	51
Figure 5.29: The Differences of the von Mises Stresses. ....	52
Figure 5.30: Tensile stresses in the x-direction. ....	53
Figure 5.31: Compressive stresses in the x-direction. ....	53
Figure 5.32: All vibration modes contour for the fully extended blade. ....	55
Figure 5.33: All vibration mode contour for the folded blade. ....	56
Figure 6.1: The comparison between blade's deflections. ....	57
Figure 6.2: The comparison between von Mises stresses for the skin only. ....	58
Figure 6.3: The comparison between von Mises stresses for the box spar only. ....	59
Figure 6.4: The comparison between stresses ( $\sigma_{zz}$ ) for the skin only. ....	59
Figure 6.5: The comparison between stresses ( $\sigma_{zz}$ ) for the box spar only. ....	60
Figure 6.6: Comparing between folded and fully extended blades stresses under gravity load. .	61
Figure 6.7: Comparing between folded and fully extended blades stresses under all load cases.	61
Figure 6.8: Transverse ( $\sigma_{xx}$ ) and von Mises stresses on folded blade edges. ....	62

## INTRODUCTION

The use of alternatives energy resources over the fossil fuel based resources is increasing. Energy sources such as wind, solar, marine energy, geothermal heat, and more have all seemed greater increase in the usage. Wind power is one type of alternative energy source that has significantly increased in the past decade. Extracting wind energy requires the use of wind turbines to convert the incident wind power into usable electricity as a typical arrangement. Despite all the renewable energy challenges and technology issues, wind energy does not pollute or leave residual waste as non-renewable energy sources do such as petroleum, coal or nuclear energy.

Generating electricity-using wind requires wind turbines. There are two types of wind turbines: vertical-axis wind turbines (VAWT) and horizontal-axis wind turbines (HAWT). Both types consist of the tower, generator, transmission shaft, rotor, and the turbine blades. The blades move under wind pressure to help to convert kinetic energy of wind to electric energy. The wind turbines are usually three-bladed and are typically over 30 meters long. The blades have low torque ripple, which contributes to excellent reliability and is usually colored white for daytime visibility by aircraft (GE Renewable Energy, 2013) (Common Wind Turbine Models, 2010). The blades rotate at 10 to 22 revolutions per minute, and at 22 rotations per minute, the speed of the blade tip exceeds 90 meters per second for blades diameter of 70 meters (GE Renewable Energy, 2013) (Common Wind Turbine Models, 2010). Also, wind turbines blades are prepared with protective features to avoid damage at high wind speeds (GE Renewable Energy, 2013) (Common Wind Turbine Models, 2010).

Due to the length of the larger blades, transporting and storing them is a design concern. One practical solution for this issue is folding the blades at some fraction of the length of the blade to save more space for storage and maintain blade efficiency. The basic idea of folded blades dates to the folding wings on aircraft used in World War II. Back then, the idea of folding the aircraft wings are to save space while storing and transporting the aircraft. The folding allows the aircraft to take less space because the folded wing usually rises over the fuselage reducing the floor area of the aircraft. In the case of folded wind turbine blades, the mechanism and structure are similar to those of folded aircraft wings. The main idea of folding the blades beside transporting and storing is to generate electricity within small wind turbine blade radius, about the two-thirds, and low-efficiency area as an important role in producing energy. Figure 1.1 presents the efficiency area for a folded blade.

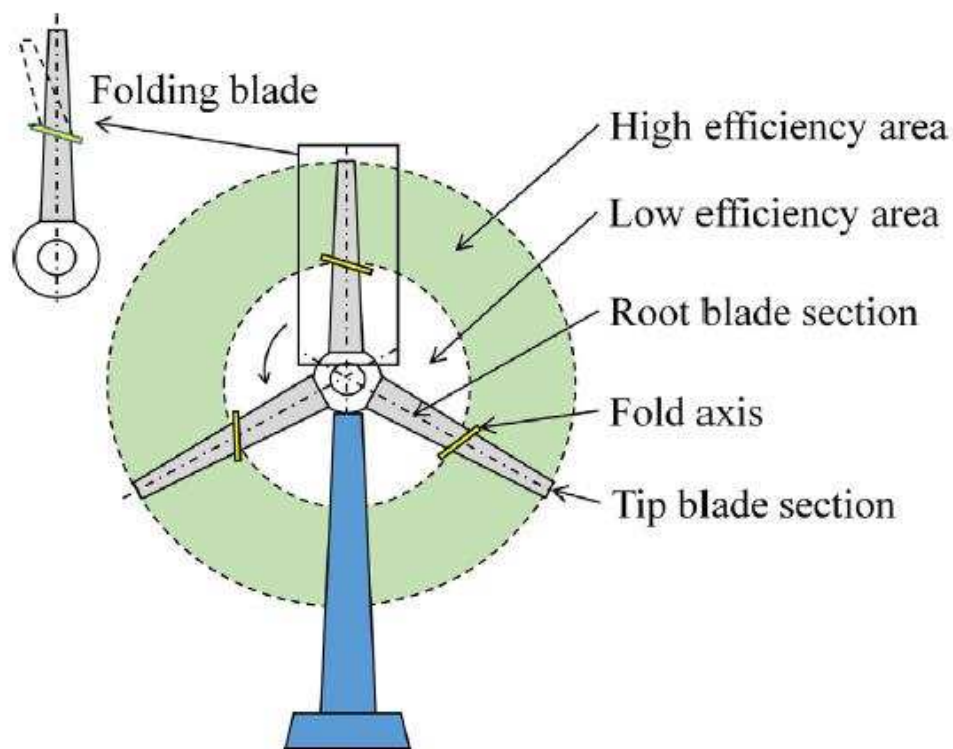


Figure 1.1: Energy efficiency areas and folded blade (Xie et al. 2015).

Folded blades are essentially what its names imply. Figure 1.2 presents a basic sketch of the conventional wind turbine blade and folded blade. Figure 1.3 helps to understand one of the blade configurations considered for analysis in this study. This geometry and several associated mechanics parameters help differentiate the behavior of the conventional and folded wind turbine blades that are the focus of this study.

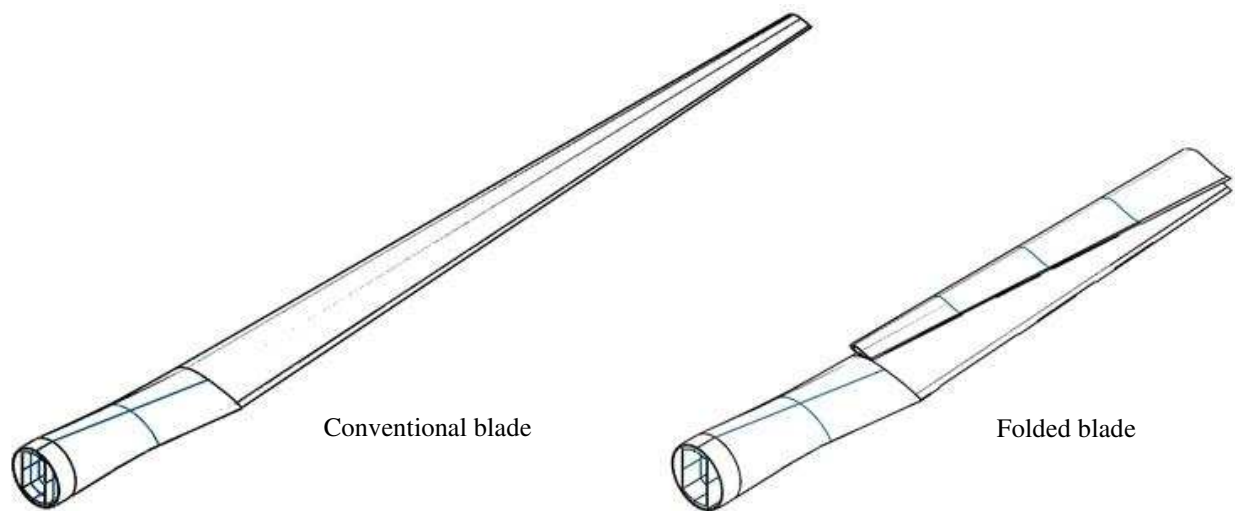


Figure 1.2: Three-dimensional sketches of conventional and folded wind turbine blade.

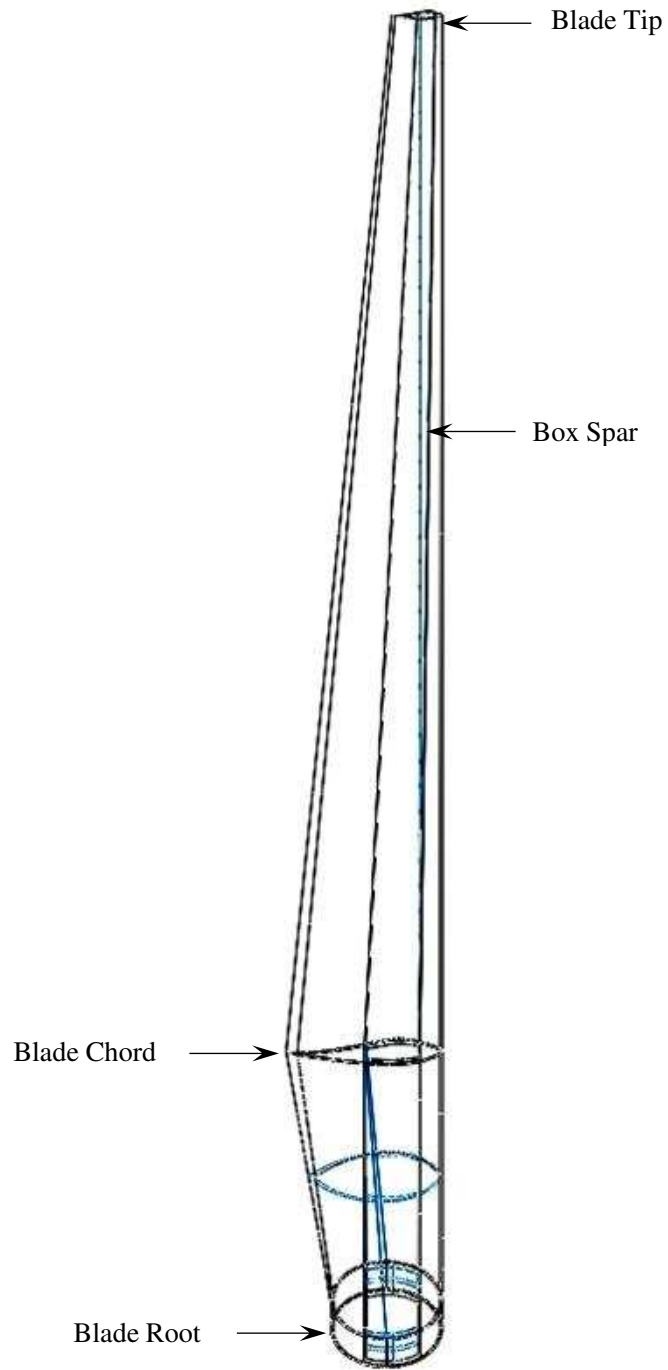


Figure 1.3: The conventional turbine blade.

This study presents typical values of static deflection, stress, and natural frequency of vibration of folded wind turbine blade in comparison to the conventional wind turbine blade. The fully conventional blade was modeled and developed for the wind turbine blade adopting an S818 airfoil shape (Griffin, 2002), and the geometry and shape were used to produce a three-dimensional finite element model of the turbine blade by using SOLIDWORKS 2016.

After generating the three-dimensional elasticity model, the geometry, material properties, and loading details were applied using ABAQUS CAE. The software ABAQUS CAE was used for all the results to compute and analyze the static deflections and stresses for two load cases (wind load and gravity load), and the free vibration analysis.

The load cases are:

1. Dead load (gravity only).
2. Dead and Live load (gravity and wind).

The first case of loading presents how much the deflections and the stresses are changing under the influence of wind load only. The second load case gives more practical results to compare between the conventional blade and folded blade for the both dead and live load. The full results include comparisons between the conventional blade and folded blade of:

1. Static deflection.
2. Longitudinal and transverse stresses.
3. The fundamental frequency of vibration.
4. Vibration modes of the blades.

## LITERATURE REVIEW

Wind turbines have been used since about 2000 B.C., starting from old windmills in ancient Babylon (Iowa Energy Center, 2014). In 1887, the first-time wind turbines began to generate electricity, which was a great achievement for Scottish academic James Blyth (Guardian, 2014). In the fall of 1941, wind turbines generated the first megawatt-class, which is known today as Smith-Putnam wind turbine (Sulzberger, 2009, and Guardian, 2014). However, generating electricity using wind power requires an increase in the size of the turbine to allow for higher performance and more power production of electricity. The Smith-Putnam wind turbine had two blades that were 75-feet long. Later, specifically in 1956, the first three-bladed wind turbines, called the Gedser Wind Turbine, was developed by Johannes Juul. This three-bladed development was a significant change in the design of the blades and has continued to be the preferred design into our present time (Guardian, 2014, and WEP, 2003).

Recently, the size of turbines started to get much bigger to allow for the higher power they needed to produce. Wind farms created to making the power generating more applicable and efficient (John, 2015). In 1980, the first known wind farm in the US began in New Hampshire and comprised of 20-30 KW turbines (Guardian, 2014). Within a minimum period, various wind farms were appearing all over the country, with more wind farms projected to constructed in onshore and offshore destinations in the coming decades (Seanergy, 2012). However, the interaction that individual turbines have with the other turbines at the wind farm create a problem, which makes it challenging to set up many wind turbines on the same farm (John, 2015). In particular, as indicated by Sørensen et al. 2008, turbulence force increments in the wakes behind every turbine while the

mean wind speed simultaneously diminishes. Consequently, the complex issue of understanding the behavior of single wind turbine to the occurrence wind turns out to be considerably more confused when considering the difference in mean wind stream and nearby turbulence (John, 2015). Understanding these interactions is an indispensable part to settle on choices in regard to the ideal arrangement and dispersing of turbines inside of a geometric space, so that power generation is improved while ensuring that the mechanical and necessary dependability of the turbine's primary framework is unaltered. At the same time, issues identified with significant deformation behavior in turbine blade reactions have developed as the length of the blades has expanded (John, 2015).

Throughout recent decades, wind turbines have been developing over length size. Turbines with an ostensible power of 10 MW rotor diameters nearing a few hundred meters are under both theoretical and efficient considerations (John, 2015). The biggest wind turbine has used with a rotor diameter is 126 m is ENERCON'S E126 7.5 MW (WPM, 2014). The blades of a turbine usually represent around 15% of the total turbine cost and are planned for covering most of the swept area (the circular area swept by the turning blades). Hence, the blades are required to be longer to guarantee a larger swept area, which allows for capturing higher wind speeds due to its higher placement on towers. Therefore, increasing the turbine blades length will cause more power generated from the wind (Johanson, 1985). At present, the variation of a rotating cantilever beam is the main idea of most of the blades designed.

In this case, the linearized stiffness for a blade under the commonly used assumption of Euler-Bernoulli beam theory is linearly associated with the product of extensional modulus multiplied by the second moment of the area. However, inversely proportional to the cube of the beam length. Since the blades increase in length, there is a stronger tendency for the beam behavior

to include nonlinear effects. Moreover, increasing the blade length could lead to a coupling between bending, torsion, and extension, which may give unexpected vibration characteristics linked to undesirable resonances. Also, this could result in elastic aero instability that causes significant concerns when increasing the length of the blade (Riziotis et al. 2004). Other concerns for turbulent wind flow include that the size of the blades and the distance between wind turbines in a farm are critical design parameters that can affect the level of wind loading along the blade length (John, 2015). The blades are exposed to a level of uniform wind flow during periods of high wind speed could produce a level of high stress that lead to fatigue damage or localized failures.

Tartibu et al. (2012) conducted modal analysis on blades similar to which of the wind turbine blades are pointing to study the relative modal change when the blades were fully extended compared to the frequencies when the blades were conventional. This study considered a straightforward model for the blade without specific geometrical shape and details, essentially considering it as a simple beam with a constant cross-section. The analysis performed treating the beam as a one-dimensional Euler-Bernoulli Beam element (Jonh, 2015). Improving on the type of simple model is one of the goals of the present study. Additional studies by (McCoy, 2006) and (Griffin, 2008) mainly focused on aerodynamic and control aspects of the turbine blade. This research included simulations using MSC-ADAMS and detailed cost modeling based on the simulated loads.

Similar considerations exist for turbulent wind streams (Moriarty et al. 2002). The size and design of the wind turbines are important design guideline could influence the level of wind pressure on the turbines along a representative column of land. The standard of relative disruption of uniform flow even past fixed objects is still a subject of intense research, and coupling the interactions of the velocity fields with rotating, and flexible turbine blades have seen a minimal

investigation. The interactions are crucial for a performance-based estimate of turbines could include optimal operating conditions, and a reasonable control of stresses may lead to fatigue damage or localized failures during periods of high wind (John, 2015).

Also, composite materials are used to reduce the extreme weight of wind turbine blades and increase their effectiveness, which also improves the fatigue life. We believe that the most intensive approach to design the wind turbine is to use the 3D finite element analysis based on brick elements. However, in the case of thin wall, 2D finite element analysis will be placed and based on the layered shell elements to extend the analysis (Chen et al. 2009). It will theoretically reduce the two number of degrees of freedom from the total that required for modeling the wind turbine blades. Therefore, finding that finite elements analysis (FEA) using the shell elements gives an unfortunate expectation of the shear stress. For example, see the FEA of a simple isotropic thin-wall cylinder (Laird et al. 2005) and the composite girder of a wind turbine blade (Pardo, and Kim 2005).

Notably, the aeroelastic analysis of the multi-body wind turbine system has to be performed to value the dynamic behavior of the blades precisely. Despite the fact that the multi-body dynamic behavior must be simulated, the aerodynamics section could simplify. The multibody dynamics simulation codes, such as ADAMS, or the industry standard of Blade Element Momentum (BEM) codes, which is more simplified, could complete the dynamic behavior of the wind turbine (Chen et al. 2009). Chen (2009) elucidate that the model reduction method is used by BEM codes to simplify the blades to a group of frequencies and mode forms. It also shows that intelligent wind turbine dynamic responses have been confirmed to be amazingly fast and reasonably correct (Chen et al. 2009). By using brick elements or shell elements, the frequencies and mode shapes could be directly gained (Chen et al. 2009). Numerous elastic modes will explain the blade behavior,

including edgewise bending, flatwise bending, and torsion, because the wind blades are thinner in one dimension more than the others. Thus, for aeroelastic analysis of the multi-body system, the FEA based on brick elements or shell elements, is not efficient even if it is valuable for obtaining detailed stress distribution (Malcom, and Laird, 2007).

In the analysis of wind turbine blade structures, shell models and the itemized 2D model are found to provide similar results for the deflection, the strain and the stress in areas arrived is 'pure bending'. On the other hand, significant variations in the studied strain and stress can happen between the shell models and the more realistic particular 2D-solid model, particularly in areas where shear directs the loading. It ought to consider when utilizing strain and stress results from shell models in the viable configuration of structures. It found that geometric nonlinearity begins to be important when displacements are of the same request as the overlay thickness (Pardo, and Kim 2005).

In addition, the increasing magnitude of blades makes transportation, manufacture, and installation of a blade difficult (Xie et al. 2015). An additional concerns that have received increased attention as turbine blades have grown in length is the difficulty of transporting the blades using open roads, highways, and rail lines. First, several countries have limits on the lengths of objects that can be transported and special permits for exceptions add to considerations and are not automatic (DoT, U.S. 2014). Second, any delays related to transportation can cause a disproportionate increase cost because of the specialized nature of turbine construction equipment. Third, transportation problems could limit the size of new turbines such as going around road corners, and narrow bridges with 35 meters blades cause an issue and could alleviate that would be making multiple-piece blades as the reporter of Swedish business Erik Palm said.



Figure 2.1: A 75 meter Siemens blade being driven over a roundabout berm in Denmark in August 2012 (Danish Television).



Figure 2.2: A 30-ton blade transported on the road across Funen and Jutland in Denmark, July 2013 (Danish Television).

As the blades grow in length, a lot of inertial and structural properties like twist bending coupling will be severely wanted better predictions (Chen et al. 2009). However, to increase the performance of wind turbines, a new design placed for the blades that provide benefits to generate power during periods of low wind speed is known as the extendable blades, which are also known as retractable turbine blades, variable length turbine blades, or telescopic blades. Pasupuleti et al. (2005), in their studies, develop a variable length wind turbine blade that can extend up to 12 m to have more power during low wind loading. In their new design, they showed that performance could improve by 44% with an increase of 20% of the blade length, which is also an improvement by about 33% of net energy production. Another study conducted by Sharma (2007) to calculate the differences between fixed turbine blades and the retractable turbine blades shows that retractable turbine blades have twice the output of energy than the other fixed-length blades. Moreover, a particular area in New Zealand found that, annually, there was an 18% increase in generating the 10 kW energy production by using wind turbine with extendable blades (Imraan et al. 2009, 2011). Also, a possible design could provide some benefit in some circumstance is the folded blades for the turbines as few studies conducted for these designs.

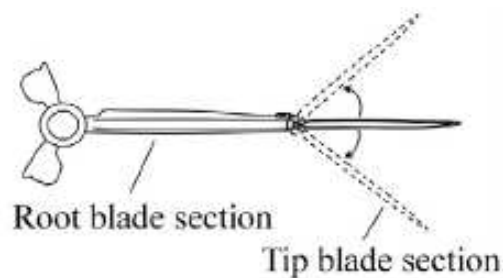


Figure 2.3: Schematic diagram of the folded blade (Xie et al. 2015).

The main characteristics of blade design are the fatigue cycling and blade bending modes. Both heavily count on the structural response to the static and transient loading. The fundamental blade frequency naturally causes the largest deflections in the blade that causes a smooth curve over the entire range of the blade length. If this frequency is close to the rotational frequency of the rotor, the caused vibrational response of the blades to simple rotational motion can cause significant capacity resonance even without any wind pressure (John, 2015). For this cause, most blades designed to the fundamental bending frequency is well over the angular frequency of the rotor. For larger blades, the frequencies and resulting mode shapes could be magnitude dependent – a condition rarely investigated in most blade designs (John, 2015). Moreover, blades subjected to caused gravitational loads as they rotate which reverse sign on either side of the rotational path and cycling stress sign at a relatively high rate. The blades are usually designed for a 20-year lifetime, allowing about 5 million cycles over the course of expected use. Again, large blades with both shear-deformable and high deformation behaviors can dramatically influence the level of stress within the blade.

There has been a significant number of studies on the nonlinear and large-deformation research of turbine blades, reaching in chronology from the historical development Hodges and Dowell (1996) for general rotor blades until the recent work of (Larsen and Nielsen, 2006). All of the previous models have established the probability of significant changes in design stresses when the beams become more flexible. Although the increased use of composites which could contain typical fiberglass elements, moving towards carbon-fiber reinforced mechanisms could yield levels of shear deformation which will dramatically change the analysis and behavior of turbine blades (John, 2015). In this research, the effects of shear deformation included by modeling the blade as an anisotropic solid.

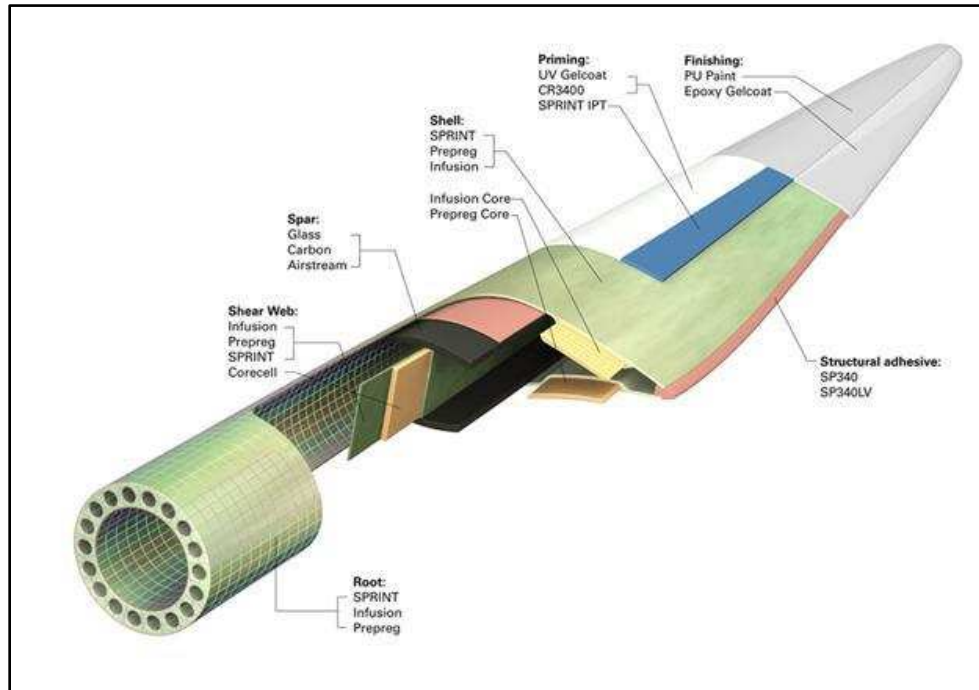


Figure 2.4: Cross-sectional details of a wind turbine blade (Stackpole, 2011).

The rotor blade mechanisms usually take advantage of the box spar designs, in which the blade skins are often manufactured separately then attached along with the structural box spar. The details configurations of the skin and box spar are shown in Figure 2.3. The spar cap and the shear web together establish the box spar. This assembly contributes the most weight for the entire blade and is responsible for the structural effectiveness and stability of the blade. Detailed diagrams included in later chapters and material components have been used, or proposed for use, for these structural elements. This study considers standard blade cross-sections that will model with continuum theories of deformation, specifically the three-dimensional equations of elasticity.

## METHODOLOGY

This chapter presents the main equations used in this study. Also, it contains the blade modeled and all the assumptions that are used. The blade model includes all the geometric details, the material properties, and various retracted blades that included for analysis. A detailed explanation of nodal displacement and fundamental frequency can derive from the primary equations.

### 3.1. Governing Equations

The equations of motion in three dimensions expressed in volume V as,

$$\begin{aligned}\frac{\partial \sigma_{xx}}{\partial x} + \frac{\partial \sigma_{yy}}{\partial y} + \frac{\partial \sigma_{zz}}{\partial z} + f_x &= \rho \frac{\partial^2 u}{\partial t^2} \\ \frac{\partial \sigma_{yx}}{\partial x} + \frac{\partial \sigma_{yy}}{\partial y} + \frac{\partial \sigma_{yz}}{\partial z} + f_y &= \rho \frac{\partial^2 v}{\partial t^2} \\ \frac{\partial \sigma_{zx}}{\partial x} + \frac{\partial \sigma_{zy}}{\partial y} + \frac{\partial \sigma_{zz}}{\partial z} + f_z &= \rho \frac{\partial^2 w}{\partial t^2},\end{aligned}\tag{3.1}$$

Where  $u(x, y, z, t)$ ,  $v(x, y, z, t)$ , and  $w(x, y, z, t)$  are the displacement in the  $x$ ,  $y$ , and  $z$  directions and  $\sigma_{xx}$ ,  $\sigma_{xy}$  and so on are the components of stress.

The strain-displacement relation is given by

$$\begin{aligned}\epsilon_x &= \frac{\partial u}{\partial x} \\ \epsilon_y &= \frac{\partial v}{\partial y}\end{aligned}$$

$$\epsilon_z = \frac{\partial w}{\partial z}$$

$$\gamma_{xy} = \frac{\partial u}{\partial y} + \frac{\partial v}{\partial x}$$

$$\gamma_{yz} = \frac{\partial v}{\partial z} + \frac{\partial w}{\partial y}$$

$$\gamma_{zx} = \frac{\partial w}{\partial x} + \frac{\partial u}{\partial z}$$

Also, The Stress-Strain relations as follows:

$$\sigma_{xx} = \sigma_x = C_{11}\epsilon_x + C_{12}\epsilon_y + C_{13}\epsilon_z$$

$$\sigma_{yy} = \sigma_y = C_{12}\epsilon_x + C_{22}\epsilon_y + C_{23}\epsilon_z \quad (3.2)$$

$$\sigma_{zz} = \sigma_z = C_{13}\epsilon_x + C_{23}\epsilon_y + C_{33}\epsilon_z$$

$$\sigma_{xy} = \tau_{xy} = C_{66}\gamma_{xy}, \quad \sigma_{yz} = \tau_{yz} = C_{44}\gamma_{yz}, \quad \text{and } \sigma_{xz} = \tau_{xz} = C_{55}\gamma_{xz}$$

For calculating the stiffness matrix, the compliance matrix used as follows:

$$[S] = \begin{bmatrix} S_{11} & S_{12} & S_{13} & 0 & 0 & 0 \\ S_{21} & S_{22} & S_{23} & 0 & 0 & 0 \\ S_{31} & S_{32} & S_{33} & 0 & 0 & 0 \\ 0 & 0 & 0 & S_{44} & 0 & 0 \\ 0 & 0 & 0 & 0 & S_{55} & 0 \\ 0 & 0 & 0 & 0 & 0 & S_{66} \end{bmatrix} = \begin{bmatrix} \frac{1}{\epsilon_x} & \frac{-v_{12}}{\epsilon_y} & \frac{-v_{13}}{\epsilon_z} & 0 & 0 & 0 \\ \frac{-v_{21}}{\epsilon_x} & \frac{1}{\epsilon_y} & \frac{-v_{23}}{\epsilon_z} & 0 & 0 & 0 \\ \frac{-v_{31}}{\epsilon_x} & \frac{-v_{32}}{\epsilon_y} & \frac{1}{\epsilon_z} & 0 & 0 & 0 \\ 0 & 0 & 0 & \frac{1}{G_{23}} & 0 & 0 \\ 0 & 0 & 0 & 0 & \frac{1}{G_{13}} & 0 \\ 0 & 0 & 0 & 0 & 0 & \frac{1}{G_{12}} \end{bmatrix}$$

Where,  $S_{12} = S_{21}$ ,  $S_{13} = S_{31}$ , and  $S_{23} = S_{32}$ .

The stiffness matrix components obtained by inverting the compliance matrix as

$$\begin{aligned}
C_{11} &= \frac{S_{33} \cdot S_{22} - S_{23}^2}{S}, & C_{22} &= \frac{S_{33} \cdot S_{11} - S_{13}^2}{S} \\
C_{33} &= \frac{S_{11} \cdot S_{22} - S_{12}^2}{S}, & C_{12} &= \frac{-(S_{12} \cdot S_{33} - S_{13} \cdot S_{23})}{S} \\
C_{13} &= \frac{-(S_{13} \cdot S_{22} - S_{12} \cdot S_{23})}{S}, & C_{23} &= \frac{-(S_{23} \cdot S_{11} - S_{12} \cdot S_{13})}{S} \\
C_{44} &= \frac{1}{S_{44}}, & C_{55} &= \frac{1}{S_{55}}, & C_{66} &= \frac{1}{S_{66}}
\end{aligned}$$

Where,

$$S = S_{11} \cdot S_{22} \cdot S_{33} - S_{11} \cdot S_{23} \cdot S_{32} - S_{22} \cdot S_{13} \cdot S_{31} - S_{33} \cdot S_{12} \cdot S_{21} - 2(S_{12} \cdot S_{23} \cdot S_{13})$$

Substituting the strain displacement and constitutive laws into the equation of motion gives

$$\frac{\partial}{\partial x} \left( C_{11} \frac{\partial u}{\partial x} + C_{12} \frac{\partial v}{\partial y} + C_{13} \frac{\partial w}{\partial z} \right) + C_{66} \frac{\partial}{\partial y} \left( \frac{\partial u}{\partial y} + \frac{\partial v}{\partial x} \right) + C_{55} \frac{\partial}{\partial z} \left( \frac{\partial w}{\partial x} + \frac{\partial u}{\partial z} \right) + f_x = \rho \frac{\partial^2 u}{\partial t^2}$$

$$C_{66} \frac{\partial}{\partial x} \left( \frac{\partial u}{\partial y} + \frac{\partial v}{\partial x} \right) + \frac{\partial}{\partial y} \left( C_{21} \frac{\partial u}{\partial x} + C_{22} \frac{\partial v}{\partial y} + C_{23} \frac{\partial w}{\partial z} \right) + C_{44} \frac{\partial}{\partial z} \left( \frac{\partial v}{\partial z} + \frac{\partial w}{\partial y} \right) + f_y = \rho \frac{\partial^2 v}{\partial t^2}$$

$$C_{55} \frac{\partial}{\partial x} \left( \frac{\partial w}{\partial x} + \frac{\partial u}{\partial z} \right) + C_{44} \frac{\partial}{\partial y} \left( \frac{\partial v}{\partial z} + \frac{\partial w}{\partial y} \right) + \frac{\partial}{\partial z} \left( C_{31} \frac{\partial u}{\partial x} + C_{32} \frac{\partial v}{\partial y} + C_{33} \frac{\partial w}{\partial z} \right) + f_z = \rho \frac{\partial^2 w}{\partial t^2}$$

The weak form of the equations of motion are obtained by multiplying each of them by arbitrary weight function  $V_i$  ( $i=1-3$ ) integrating over the volume of a typical element, and setting the result to zero:

$$\int_V v_1 \left( \frac{\partial}{\partial x} \left( C_{11} \frac{\partial u}{\partial x} + C_{12} \frac{\partial v}{\partial y} + C_{13} \frac{\partial w}{\partial z} \right) + C_{66} \frac{\partial}{\partial y} \left( \frac{\partial u}{\partial y} + \frac{\partial v}{\partial x} \right) + C_{55} \frac{\partial}{\partial z} \left( \frac{\partial w}{\partial x} + \frac{\partial u}{\partial z} \right) + f_x - \left( \rho \frac{\partial^2 u}{\partial t^2} \right) \right) dx dy dz = 0$$

$$\int_V v_2 \left( C_{66} \frac{\partial}{\partial x} \left( \frac{\partial u}{\partial y} + \frac{\partial v}{\partial x} \right) + \frac{\partial}{\partial y} \left( C_{21} \frac{\partial u}{\partial x} + C_{22} \frac{\partial v}{\partial y} + C_{23} \frac{\partial w}{\partial z} \right) + C_{44} \frac{\partial}{\partial z} \left( \frac{\partial v}{\partial z} + \frac{\partial w}{\partial y} \right) + f_y - \left( \rho \frac{\partial^2 v}{\partial t^2} \right) \right) dx dy dz = 0$$

$$\int_V v_3 \left( C_{55} \frac{\partial}{\partial x} \left( \frac{\partial w}{\partial x} + \frac{\partial u}{\partial z} \right) + C_{44} \frac{\partial}{\partial y} \left( \frac{\partial v}{\partial z} + \frac{\partial w}{\partial y} \right) + \frac{\partial}{\partial z} \left( C_{31} \frac{\partial u}{\partial x} + C_{32} \frac{\partial v}{\partial y} + C_{33} \frac{\partial w}{\partial z} \right) + f_z - \left( \rho \frac{\partial^2 w}{\partial t^2} \right) \right) dx dy dz = 0$$

Integration by parts and use of the divergence theorem yields

$$\int_V \left( C_{11} \frac{\partial v_1}{\partial x} \frac{\partial u}{\partial x} + C_{12} \frac{\partial v_1}{\partial x} \frac{\partial v}{\partial y} + C_{13} \frac{\partial v_1}{\partial x} \frac{\partial w}{\partial z} + C_{66} \frac{\partial v_1}{\partial y} \frac{\partial u}{\partial y} + C_{66} \frac{\partial v_1}{\partial y} \frac{\partial v}{\partial x} + C_{55} \frac{\partial v_1}{\partial z} \frac{\partial w}{\partial x} + C_{55} \frac{\partial v_1}{\partial z} \frac{\partial u}{\partial z} + f_x \cdot v_1 - \left( \rho \frac{\partial^2 u}{\partial t^2} \right) \cdot v_1 \right) dx dy dz - \oint_r v_1(t_x) ds = 0$$

$$\int_V \left( C_{66} \frac{\partial v_2}{\partial x} \frac{\partial u}{\partial y} + C_{66} \frac{\partial v_2}{\partial x} \frac{\partial v}{\partial x} + C_{21} \frac{\partial v_2}{\partial y} \frac{\partial u}{\partial x} + C_{22} \frac{\partial v_2}{\partial y} \frac{\partial v}{\partial y} + C_{23} \frac{\partial v_2}{\partial y} \frac{\partial w}{\partial z} + C_{44} \frac{\partial v_2}{\partial z} \frac{\partial v}{\partial z} \right. \\ \left. + C_{44} \frac{\partial v_2}{\partial z} \frac{\partial w}{\partial y} + f_y \cdot v_2 - \left( \rho \frac{\partial^2 v}{\partial t^2} \right) \cdot v_2 \right) dx dy dz - \oint_r v_2(t_y) ds = 0 \quad (3.3)$$

$$\int_V \left( C_{55} \frac{\partial v_3}{\partial x} \frac{\partial w}{\partial x} + C_{55} \frac{\partial v_3}{\partial x} \frac{\partial u}{\partial z} + C_{44} \frac{\partial v_3}{\partial y} \frac{\partial v}{\partial z} + C_{44} \frac{\partial v_3}{\partial y} \frac{\partial w}{\partial y} + C_{31} \frac{\partial v_3}{\partial z} \frac{\partial u}{\partial x} + C_{32} \frac{\partial v_3}{\partial z} \frac{\partial v}{\partial y} \right. \\ \left. + C_{33} \frac{\partial v_3}{\partial z} \frac{\partial w}{\partial z} + f_z \cdot v_3 - \left( \rho \frac{\partial^2 w}{\partial t^2} \right) \cdot v_3 \right) dx dy dz - \oint_r v_3(t_z) ds = 0$$

Here the components of the stress function vector are given as

$$t_x = \left( C_{11} \frac{\partial u}{\partial x} + C_{12} \frac{\partial v}{\partial y} + C_{13} \frac{\partial w}{\partial z} \right) \cdot n_x + \left( C_{66} \frac{\partial u}{\partial y} + C_{66} \frac{\partial v}{\partial x} \right) \cdot n_y + \left( C_{55} \frac{\partial w}{\partial x} + C_{55} \frac{\partial u}{\partial z} \right) \cdot n_z$$

$$t_y = \left( C_{66} \frac{\partial u}{\partial y} + C_{66} \frac{\partial v}{\partial x} \right) \cdot n_x + \left( C_{21} \frac{\partial u}{\partial x} + C_{22} \frac{\partial v}{\partial y} + C_{23} \frac{\partial w}{\partial z} \right) \cdot n_y + \left( C_{44} \frac{\partial v}{\partial z} + C_{44} \frac{\partial w}{\partial y} \right) \cdot n_z$$

$$t_z = \left( C_{55} \frac{\partial w}{\partial x} + C_{55} \frac{\partial u}{\partial z} \right) \cdot n_x + \left( C_{44} \frac{\partial v}{\partial z} + C_{44} \frac{\partial w}{\partial y} \right) \cdot n_y + \left( C_{31} \frac{\partial u}{\partial x} + C_{32} \frac{\partial v}{\partial y} + C_{33} \frac{\partial w}{\partial z} \right) \cdot n_z$$

The boundary conditions specified as

- NBCs (Natural Boundary Conditions): Specify  $t_x$ ,  $t_y$ , or  $t_z$ .
- EBCs (Elastic Boundary Conditions): Specify  $u$ ,  $v$ , or  $w$ .

At every boundary, we would know  $u$  or  $t_x$ ,  $v$  or  $t_y$ , and  $w$  or  $t_z$ .

For the free vibration problem, we initially approximate  $u$ ,  $v$ , and  $w$  as having periodic motion as shown,

$$u(x, y, z, t) = u(x, y, z) \sin \omega t$$

$$v(x, y, z, t) = v(x, y, z) \sin \omega t$$

$$w(x, y, z, t) = w(x, y, z) \sin \omega t$$

For conventional finite element approximations, the displacements for the static response with the temporal constraints removed, and the weighting function  $v_1$ ,  $v_2$ ,  $v_3$  approximated as below.

$$u = \sum_{j=1}^n n_j \psi_j^u, \quad v = \sum_{j=1}^n v_j \psi_j^v, \quad w = \sum_{j=1}^n w_j \psi_j^w$$

Where,

$$v_1 = \psi_i^u, \quad v_2 = \psi_i^v, \quad v_3 = \psi_i^w$$

Substituting this into the weak form as yields

$$K_{ij}^{11} u_i + K_{ij}^{12} v_i + K_{ij}^{13} w_i = F_i^1 + \omega^2 M_{ij}^{11} u_i$$

$$K_{ij}^{21} u_i + K_{ij}^{22} v_i + K_{ij}^{23} w_i = F_i^2 + \omega^2 M_{ij}^{22} v_i$$

$$K_{ij}^{31} u_i + K_{ij}^{32} v_i + K_{ij}^{33} w_i = F_i^3 + \omega^2 M_{ij}^{33} w_i$$

In matrix form,

$$\begin{bmatrix} [K^{11}] & [K^{12}] & [K^{13}] \\ [K^{21}] & [K^{22}] & [K^{23}] \\ [K^{31}] & [K^{32}] & [K^{33}] \end{bmatrix} \begin{Bmatrix} \{u\} \\ \{v\} \\ \{w\} \end{Bmatrix} = \begin{Bmatrix} \{F^1\} \\ \{F^2\} \\ \{F^3\} \end{Bmatrix} - \omega^2 \begin{bmatrix} [M^{11}] & [0] & [0] \\ [0] & [M^{22}] & [0] \\ [0] & [0] & [M^{33}] \end{bmatrix} \begin{Bmatrix} \{u\} \\ \{v\} \\ \{w\} \end{Bmatrix} \quad (3.4)$$

Where the global

Stiffness matrix gave as

$$\begin{bmatrix} [K^{11}] & [K^{12}] & [K^{13}] \\ [K^{21}] & [K^{22}] & [K^{23}] \\ [K^{31}] & [K^{32}] & [K^{33}] \end{bmatrix}$$

The corresponding elements of the matrix are,

$$K_{ij}^{11} = \int_V \left( C_{11} \frac{\partial \psi_i^u}{\partial x} \frac{\partial \psi_j^u}{\partial x} + C_{66} \frac{\partial \psi_i^u}{\partial y} \frac{\partial \psi_j^u}{\partial y} + C_{55} \frac{\partial \psi_i^u}{\partial z} \frac{\partial \psi_j^u}{\partial z} \right) dx dy dz$$

$$K_{ij}^{12} = \int_V \left( C_{12} \frac{\partial \psi_i^u}{\partial x} \frac{\partial \psi_j^v}{\partial y} + C_{66} \frac{\partial \psi_i^u}{\partial y} \frac{\partial \psi_j^v}{\partial x} \right) dx dy dz$$

$$K_{ij}^{13} = \int_V \left( C_{13} \frac{\partial \psi_i^u}{\partial x} \frac{\partial \psi_j^w}{\partial z} + C_{55} \frac{\partial \psi_i^u}{\partial z} \frac{\partial \psi_j^w}{\partial x} \right) dx dy dz$$

$$K_{ij}^{21} = \int_V \left( C_{66} \frac{\partial \psi_i^v}{\partial x} \frac{\partial \psi_j^u}{\partial y} + C_{21} \frac{\partial \psi_i^v}{\partial y} \frac{\partial \psi_j^u}{\partial x} \right) dx dy dz$$

$$K_{ij}^{22} = \int_V \left( C_{66} \frac{\partial \psi_i^v}{\partial x} \frac{\partial \psi_j^v}{\partial x} + C_{22} \frac{\partial \psi_i^v}{\partial y} \frac{\partial \psi_j^v}{\partial y} + C_{44} \frac{\partial \psi_i^v}{\partial z} \frac{\partial \psi_j^v}{\partial z} \right) dx dy dz$$

$$K_{ij}^{23} = \int_V \left( C_{23} \frac{\partial \psi_i^v}{\partial y} \frac{\partial \psi_j^w}{\partial z} + C_{44} \frac{\partial \psi_i^v}{\partial z} \frac{\partial \psi_j^w}{\partial y} \right) dx dy dz$$

$$K_{ij}^{31} = \int_V \left( C_{55} \frac{\partial \psi_i^w}{\partial x} \frac{\partial \psi_j^u}{\partial z} + C_{31} \frac{\partial \psi_i^w}{\partial z} \frac{\partial \psi_j^u}{\partial x} \right) dx dy dz$$

$$K_{ij}^{32} = \int_V \left( C_{44} \frac{\partial \psi_i^w}{\partial y} \frac{\partial \psi_j^v}{\partial z} + C_{32} \frac{\partial \psi_i^w}{\partial z} \frac{\partial \psi_j^v}{\partial y} \right) dx dy dz$$

$$K_{ij}^{33} = \int_V \left( C_{55} \frac{\partial \psi_i^w}{\partial x} \frac{\partial \psi_j^w}{\partial x} + C_{44} \frac{\partial \psi_i^w}{\partial y} \frac{\partial \psi_j^w}{\partial y} + C_{33} \frac{\partial \psi_i^w}{\partial z} \frac{\partial \psi_j^w}{\partial z} \right) dx dy dz$$

The mass matrix elements gave as

$$\begin{bmatrix} [M^{11}] & [0] & [0] \\ [0] & [M^{22}] & [0] \\ [0] & [0] & [M^{33}] \end{bmatrix}$$

Where

$$M_{ij}^{11} = \int_V \rho \psi_i^u \psi_j^u dx dy dz$$

$$M_{ij}^{22} = \int_V \rho \psi_i^v \psi_j^v dx dy dz$$

$$M_{ij}^{33} = \int_V \rho \psi_i^w \psi_j^w dx dy dz$$

Finally, the force factor is given by

$$\begin{Bmatrix} \{F^1\} \\ \{F^2\} \\ \{F^3\} \end{Bmatrix}$$

Where

$$F_i^1 = \int_V f_x \psi_i^u dx dy dz + \oint_r t_x \psi_i^u ds$$

$$F_i^2 = \int_V f_y \psi_i^v dx dy dz + \oint_r t_y \psi_i^v ds$$

$$F_i^3 = \int_V f_z \psi_i^w dx dy dz + \oint_r t_z \psi_i^w ds$$

The matrix equation for computing the static deflection is in the absence of dynamic effects is found by setting the frequency to zero, resulting in

$$\begin{bmatrix} [K^{11}] & [K^{12}] & [K^{13}] \\ [K^{21}] & [K^{22}] & [K^{23}] \\ [K^{31}] & [K^{32}] & [K^{33}] \end{bmatrix} \begin{Bmatrix} \{u\} \\ \{v\} \\ \{w\} \end{Bmatrix} = \begin{Bmatrix} \{F^1\} \\ \{F^2\} \\ \{F^3\} \end{Bmatrix} \quad (3.5)$$

For free vibrations, fundamental frequency analysis does not include external loading.

Therefore, the force vector equals zero. Hence the matrix equation, for calculating free vibration is given by

The equation is in the form

$$[A]\{X\} = \lambda[B]\{X\}$$

Which is a generalized eigenvalue problem, which can be solved by conventional methods.

### **3.2. Blade Material and Geometry:**

The blade model was generated using SolidWorks 2016, analyzed using Abaqus CAE and modeled according to a study conducted by Sandia National Laboratory (Griffin, 2002). Several details were assumed:

- A glass fiber composite was assumed for all blade properties, and solid elements were used to model the blade.
- The pressure and wind load were assumed to be distributed consistently along the length of the blade depending on the orientation and elevation.
- The carbon fiber material properties were considered for the skin, and the glass fiber material properties were used for the box spar inside the skin.
- The blade thicknesses are dependent on the area of the blade.

The blade model of Griffin (2002) has an S818 airfoil shape with a length of 100 m. The cross-section is shown in Figure 3.1. In this study, the same blade was used with an S818 airfoil shape and 35 m length for analysis. The blade was designed in two parts: the box spar and the skin that covers the box spar. The box spar is considered the primary structural element of the blade, which is required for strength and rigidity. The box spar is covered then by a thin layer of skin which has specific dimensions and specific material properties as shown in Figure 3.1.

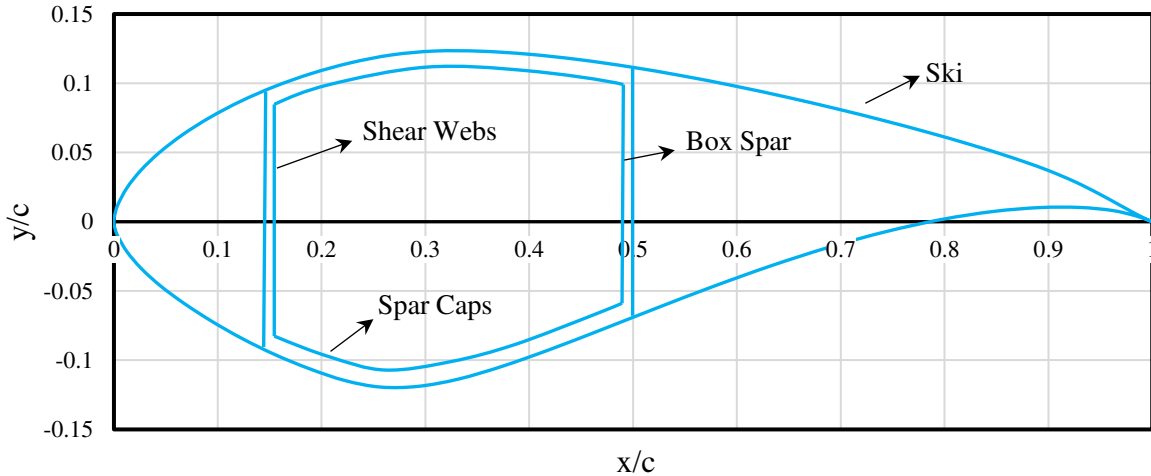


Figure 3.1: The NREL's S818 Airfoil.

Figure 3.1 shows the blade planform profile along the long axis. The parameters in the graph are expressed relative to this dimension. As shown, the maximum airfoil width is located at 25% of  $r/R$  to the tip of the blade, and the blade root was determined at 5% of  $r/R$  and remained circular to 7% of  $r/R$ . The S818 airfoil planform profile as shown in Figure 3.2 was used in our model. Where,  $R$  is the radius rotation of the blade, as equal here to 35 meters, and  $c$  is the largest width of the Airflo shape. The blade length from the maximum airfoil width to the tip is equal to 26.25 m. Figure 3.1 also shows the S818 airfoil profile dimensions at the maximum chord and detailed aspects of the box spar.

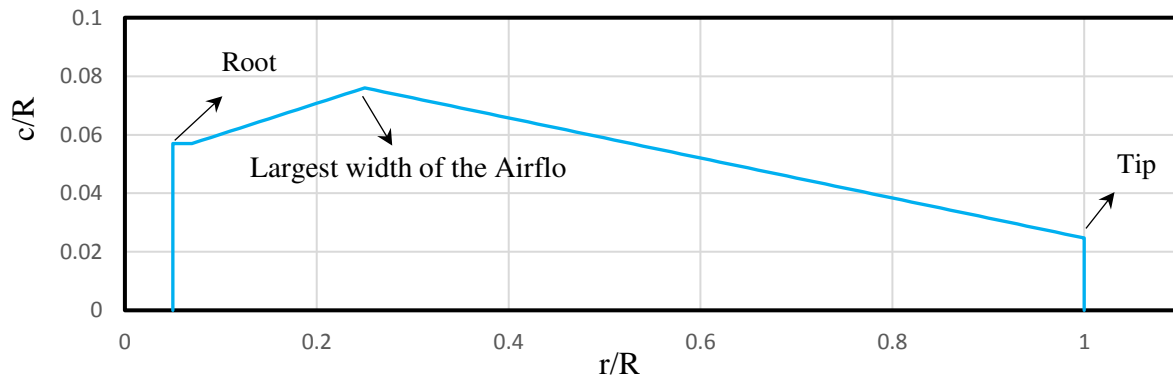


Figure 3.2: The blade planform profile.

From the blade planform profile data, the dimensions are assumed as follows: the blade has a length of 35 m from the center of the rotor to the tip and 33.25 m from the root location to the tip. The blade remains circular with a diameter of 2 m to 0.7 m length, before transitioning to an airfoil shape at 6.3 m. At this location, the airfoil shape has the maximum chord length of 2.84 m and remains in airfoil shape to the tip of the blade, at which the minimum chord length is 0.91 m. This blade was specifically modeled to compare and compute the static deflection and the stresses under a variety of wind load pressure for the folded and extended lengths, but it did not a model for detailed blade design within laminate layers. The blade detail assumptions such as the layers of polymer used and the thickness of the box spar and the skin will be specified below.

### **3.2.1. The Box Spar Details**

The box spar consists of shear webs and the spar caps as shown in Figure 3.1. The top and bottom surface of the fully extended blade connect as a box throughout the blade length as shown in Figure 3.1. The box material is assumed to made of poly glass fiber (John, 2015) with the material properties of Table 3.1. Features such as lightweight, high strength, and high structural rigidity indicate that carbon fiber is an ideal material for the box spar. The shear webs have a thickness of 2 cm at the root and 1.2 cm at the maximum length of the airfoil section and through 0.39 cm at the end of the box. For the spar caps, both top and bottom faces have a thickness of 10 cm at the root, and 8 cm at the largest length of the airfoil section tapers and up to 2.6 cm at the tip of the box see Figure 3.3.

### **3.2.2. The Skin Details**

Table 3.1 also shows the material properties of the skin. This surface surrounds the box spar, which ensures the needed strength and structural integrity while adding the torsional resistance of the blade. The skin was assumed to have a thickness of 5 cm at the root and 10 mm

at the maximum length of the airfoil section through 2 mm at the end of the skin. The objective of using these materials and geometry was to present a representative design that was used actual turbine blades. Therefore, these material properties and geometries are representative of typical blades. Also, Figure 3.3 presents the connection between the skin and the box spar.

### **3.3. The Folded Blade Details**

The folded blade consists of two sections as shown in Figure 3.4. The first section consists of the box spar and the skin which was assumed to have a length of approximately two-thirds of the total blade original length of 33.25 m (20 m). The second section consists of the rest of the blade which is the box spar and skin that has a length of 13.25 m folded above the first section. Four fixed hinges connect at the cutting edges of both sections. The length of the cutting edges is 2 m, and the two edges are connected at 0.605 m by four fixed hinges with 0.2 meters between them, to ensure that the folded section will move as one body with the other part of the blade. Table 3.1 shows the material properties used for the folded blade. Details on the type of connection were not considered in this study.

### **3.4. Finite Element Model**

In the finite element analysis for the entire model, the blade was divided into 55534, and 91957 nodes located together at the central locations in the element for the original blade length and connected appropriately. The element material and structural properties are given according to Table 3.1. All elements are eight-nodded brick elements. The directions of the blade's axes showed in Figure 3.5.

Table 3.1: Material Properties of Poly-Carbon Fiber and Glass Fiber for Blade Modeling (Performance Composites, 2014).

Material	Poly-Glass Fiber	Poly-Carbon Fiber
Density	1900 Kg/m <sup>3</sup>	1600 Kg/m <sup>3</sup>
E <sub>x</sub>	40,000 MPa	135,000 MPa
E <sub>y</sub>	8000 MPa	10,000 MPa
E <sub>z</sub>	8000 MPa	10,000 MPa
$\nu_{yz}$	0.5	0.6
$\nu_{xz}$	0.25	0.3
$\nu_{xy}$	0.25	0.3
G <sub>yz</sub>	3000 MPa	3,750 MPa
G <sub>xz</sub>	4000 MPa	5000 MPa
G <sub>xy</sub>	4000 MPa	5000 MPa

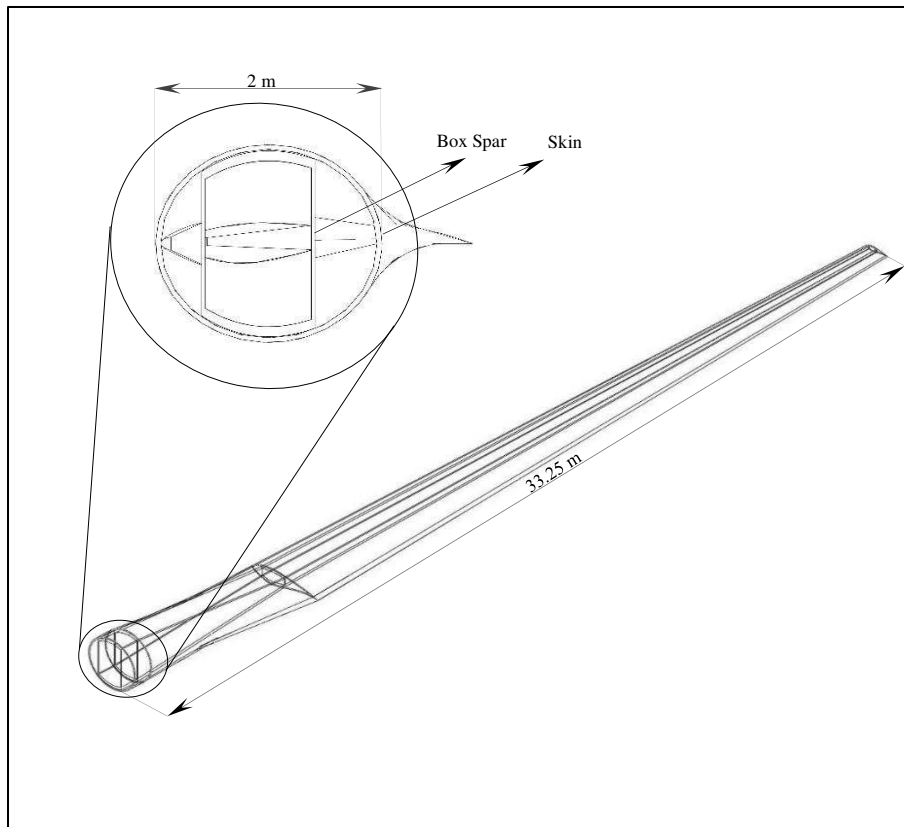


Figure 3.3: The connection between the skin and the box spar.

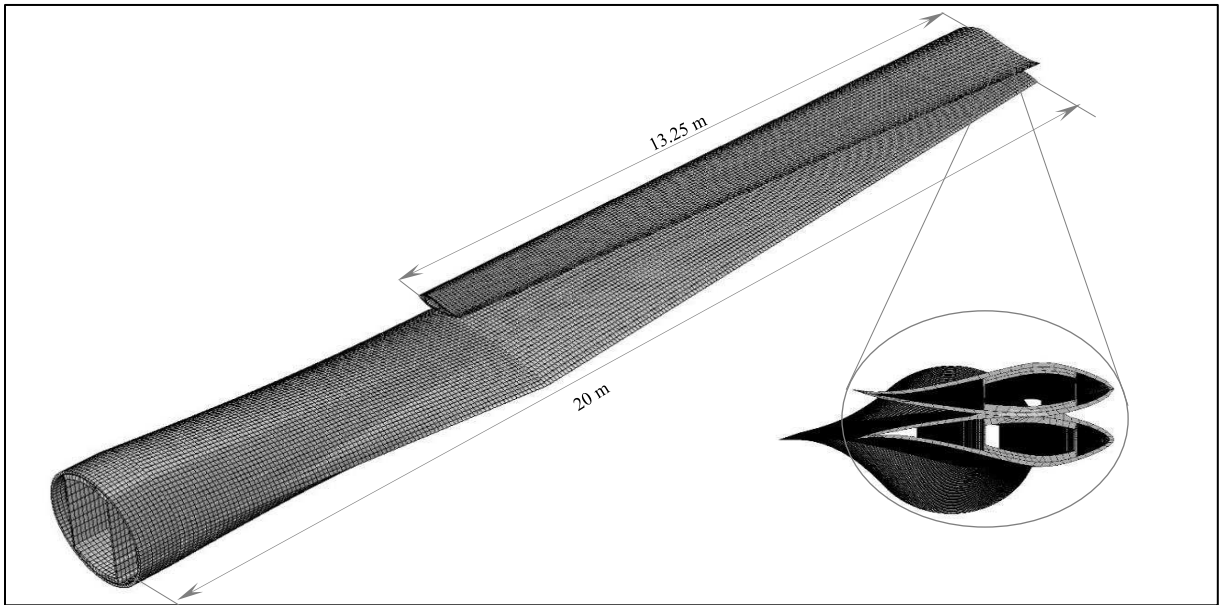


Figure 3.4: The folded blade.

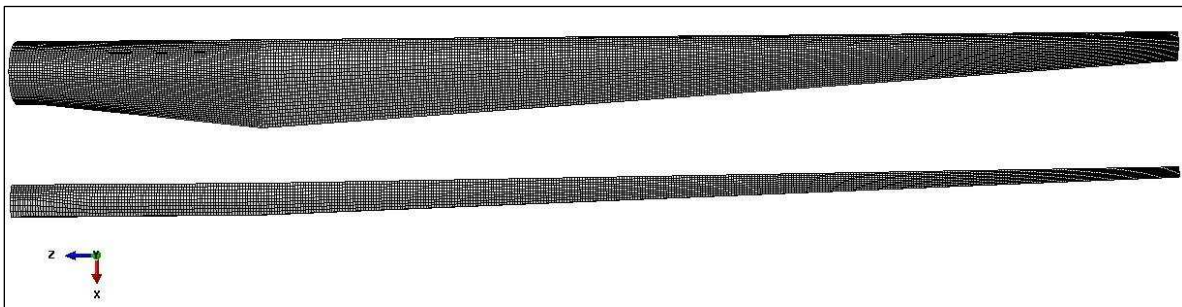


Figure 3.5: Axes of the blade model.

## ANALYSIS

### 4.1. Static Deflection Calculations

This chapter describes the loadings of the static deflection cases of the wind turbine blade under a combined wind load along with blade weight that considered as a dead load of the blade. The required stresses are also described, along with the calculation of natural frequencies for both blades. This analysis intends to determine the key differences in field vibration between the folded and fully extended blade configurations.

#### 4.1.1. Wind Load (Live Loading)

The blades were subjected to wind pressure under fully extended positions, assuming a wind speed of 11 meters per second (Jonkman et al., 2009). This speed is needed to calculate the wind force and loading along the blade length.

As the blade rotates, the maximum wind load acts at the root of the blade when the position of the blade is below the hub. Also, the maximum wind load acts at the tip of the blade when the position of the blade is above hub height. It shows that the wind pressure magnitude varies through the blade length. However, the assumption for the wind speed is to be a constant of 11 m/s from the root to the blade tip.

The wind pressure can complete from the wind velocity by using Bernoulli's equation for pressure equilibrium, or

$$P = \frac{1}{2} \cdot \rho \cdot v^2$$

Here,

$P$  = Wind pressure (MPa)

$\rho$  = Density of air =  $1.2754 \text{ kg/m}^3$ , and

$v$  = Incident wind velocity.

As a standard procedure, the effective areas of the blade surface were used to place the equivalent load at each node. Knowing the area of each element and the wind loads allow calculating the wind pressure for each node, which acts in the positive  $z$ -direction. In equation 3.3, the force vector includes all loads by internal and external forces. Any term in the vector consists of body force and surface loading acting on the corresponding element. The wind loading accounted for in the analysis as the surface terms in the Force Vector of equation 3.3, represents the wind loading on the beam.

#### **4.1.2. Gravity Load (Dead Load)**

The gravity load is computed and acts independently at each node as representing a uniformly distributed load over the blade length. The mass density can differ depending on the blade material. The gravity load accounted for the force vectors of the equation 3.3 acts as an integrated body force at the nodal locations.

As is explained above, Figure 4.1, 4.2, and 4.3 present the load efficient on the blades on the maximum effect on the blade  $y$ -direction and while the blade is rotating. Figure 4.1 presents both the fully extended and folded blades under the cases of loads (yellow arrows present the dead load, and the purple arrows present the wind load). In addition, Figure 4.2 and 4.3 present the wind and the dead loads affecting both the fully extended and folded blades.



Figure 4.1: Fully extended and folded blade under both load cases.

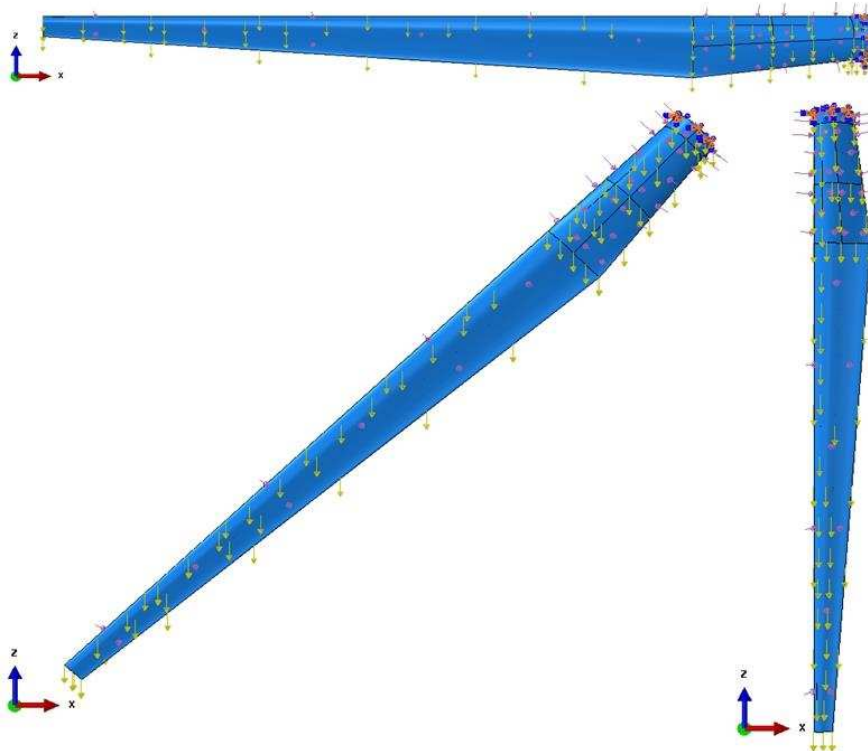


Figure 4.2: Fully extended blade under both load cases while rotating.

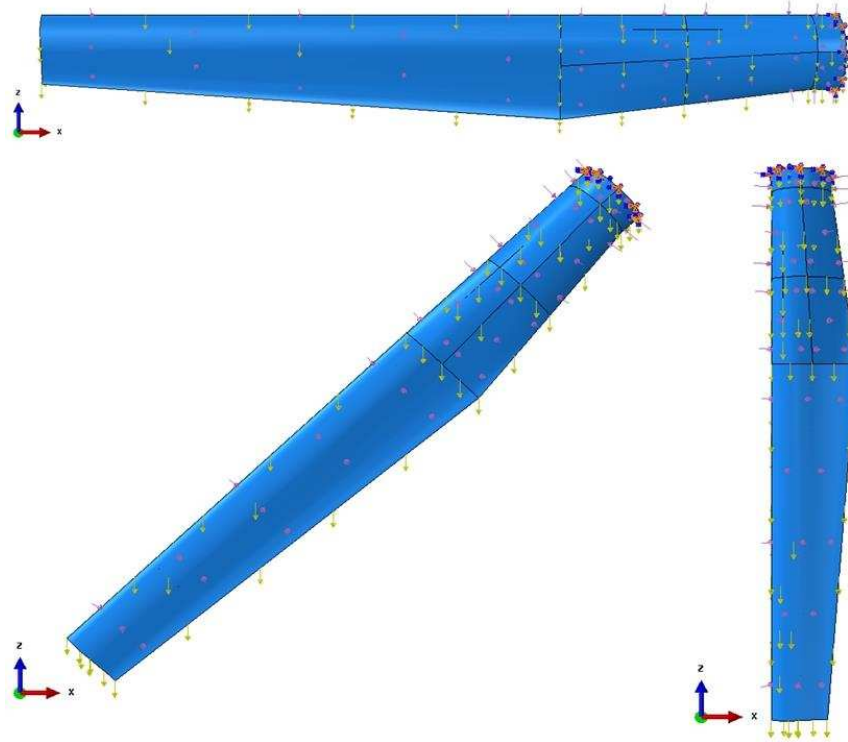


Figure 4.3: Folded blade under both load cases while rotating.

#### 4.2. Deflections Calculations

The displacement vector is computed using the stiffness matrix and force vectors formed using equation 3.5. Following the element assembly of the element stiffness matrices and force vectors for each of the elements of the global force vectors and global stiffness matrix respectively, this linear system can be solved for the nodal displacements.

The displacements are computed using the output of the analysis of these global matrices consists of the displacements occurring for each node. The set of nodes that were selected to represent blade displacement is in a straight line along the blade length within the movement in the y-direction. Figure 4.1 presents the coordinates of the nodes selected for static displacements.

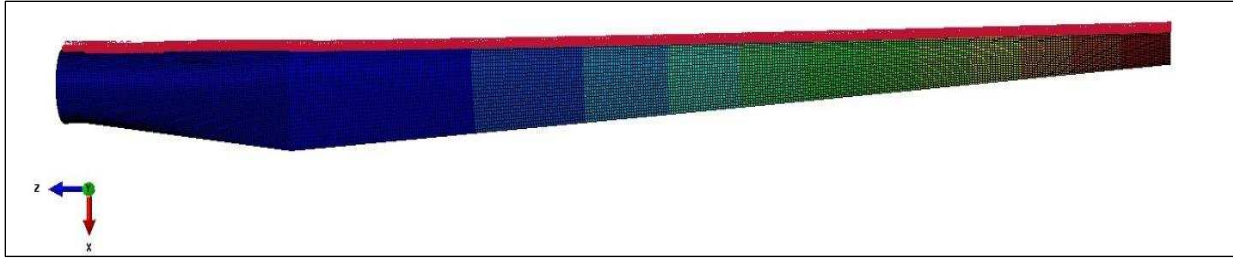


Figure 4.4: Coordinates of the nodes selected for static displacements.

### 4.3. Stresses Calculations

After calculating the displacements, the stresses can be calculated for both the conventional and the folded blades. All the stresses were computed at the Gauss points. Displacement gradients and strains are calculated at the Gauss point first, and then equation 3.2 is employed to calculate the stress in both the longitudinal and the transverse direction of the blade, ( $\sigma_{xx}$ ) and ( $\sigma_{xz}$ ) respectively. In this study, the longitudinal axis is the z-axis, and the axial stresses are denoted as ( $\sigma_{zz}$ ), and the transverse shear stresses are ( $\sigma_{xz}$ ). ABAQUS CAE computes all the deflections and the stresses of all the nodes and the elements as shown in the next chapter.

### 4.4. Frequency and Model Shape Calculations

Assembly of the matrices and the details of weak form equations for the free vibration can be demonstrated in the methodology's chapter. For free vibration calculations, only the stiffness and mass matrices are considered and not the force vector. The lowest frequencies and the mode shapes of vibration are then calculated using ABAQUS CAE software via the generalized eigenvalue problem. Based on this calculation, the fundamental frequency is the lowest non-zero eigenvalue, and the vibrational modes of the blade are the corresponding non-zero eigenvectors. The vibrational modes and frequencies of each of conventional and folded blades are summarized in the next chapter.

## RESULTS

In this chapter, the key results are presented for the static dead load case, the static dead plus live load case, and the free vibration analysis. In all cases, the focus is on the differences between the field variables for the two configurations of the conventional and folded blades.

### 5.1. Dead Load Case

#### 5.1.1. Static Deflection for the Blade

The static deflection of the conventional blade is measured at the blade surface under the dead load only from the body force vector within the blade volume. The horizontal axis shows the blade length in meters and the vertical axis presents the deflection along the length. Figure 5.2 shows the deflection and the von Mises contours for the fully extended blade and indicate the locations of the maximum displacement and stress in the blade section.

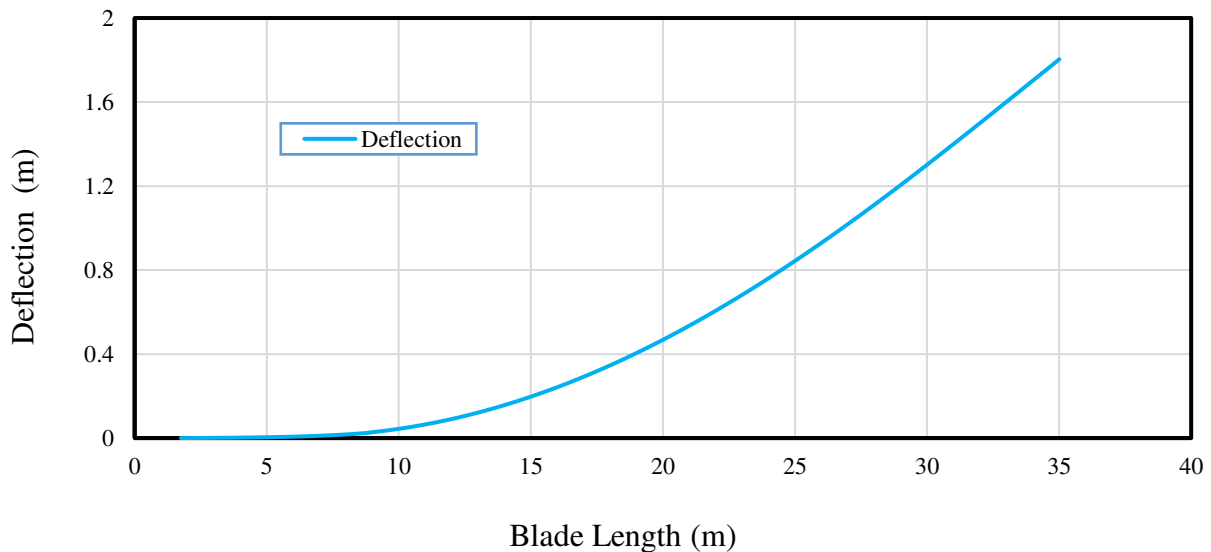


Figure 5.1: Static deflection for the fully extended blade.

### 5.1.2. Stresses in the Blade Skin

The value of von Mises stress at the skin surface is shown in Figure 5.3, for each tension and compression surfaces under the pressure of the dead load only. The horizontal axis presents the skin length in meters, and the vertical axis shows the von Mises stress in each skin section. The highest value of von Mises stress is located at the largest width of the airfoil cross-sectional in the x-direction for each surface as shown in Figure 5.3. The differences between the two graphs are regarding the load that is placing at the tension surface of the skin. Because of the gravity pressure is applying on the tension surface of the skin (y-direction), which leads to about a 5% difference between the stress distributions.

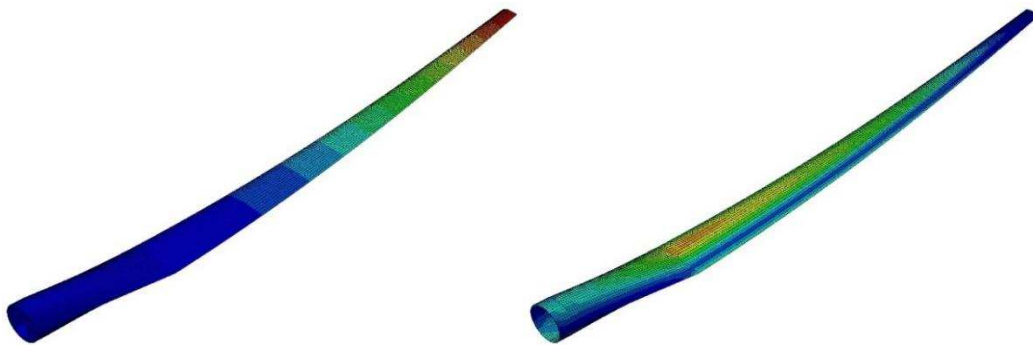


Figure 5.2: The deflected and the von Mises contour for the fully extended blade.

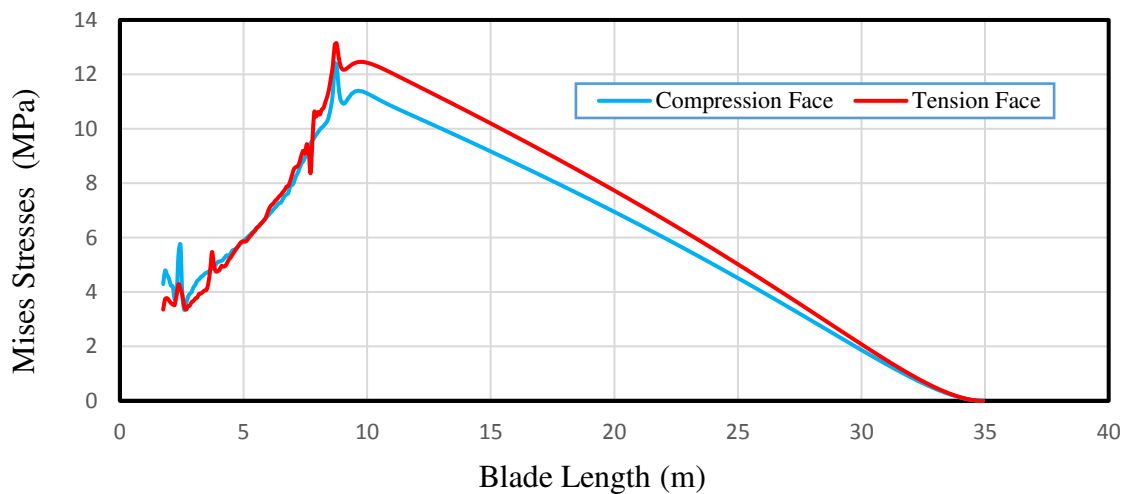


Figure 5.3: The von Mises stresses for the fully extended blade.

Figures 5.4, and 5.5 show each of the axial stresses ( $\sigma_{zz}$ ) acting on all skin sections as a function of length. This component represents the typical bending stress in the blade and is likely the dominant stress component in the entire blade surfaces. As shown, each of the maximum tension and compression stresses takes place at the largest width of the airfoil cross-sectional in the x-direction. The vertical axis presents the tension and compression stresses in MPa, and the horizontal axis presents the skin length in meters. Figure 5.6 shows the stress contours for ( $\sigma_{zz}$ ) for the fully extended blade.

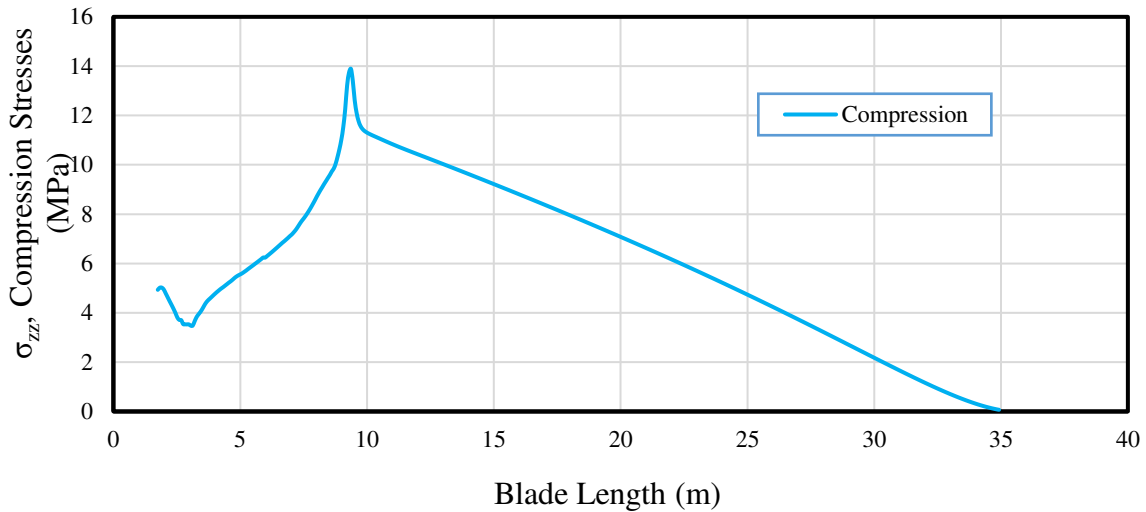


Figure 5.4: Compression stresses in the z-direction for the fully extended blade surface.

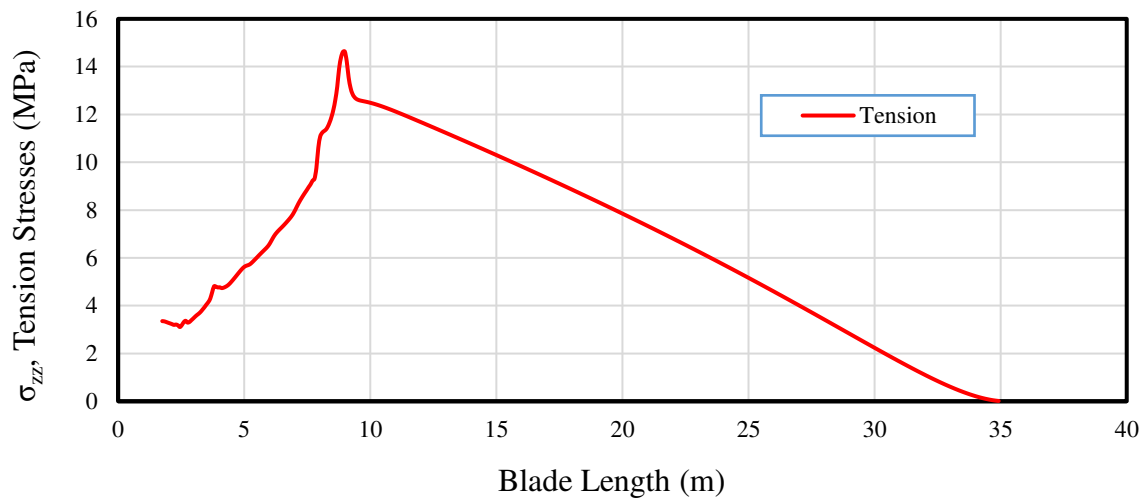


Figure 5.5: Tensile stress in the z-direction for the fully extended blade surface.

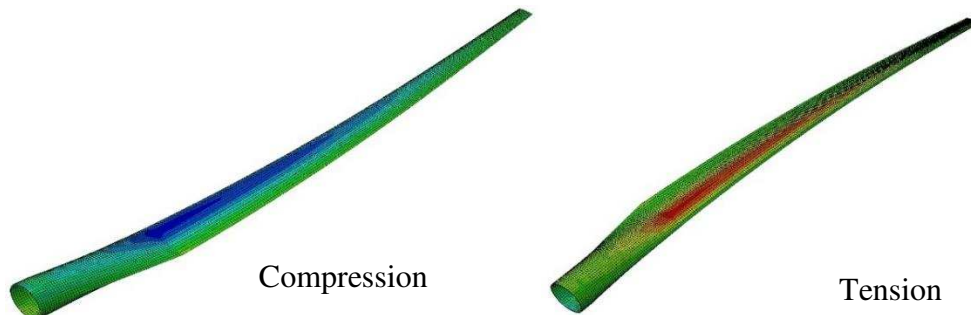


Figure 5.6: The stresses contour for ( $\sigma_{zz}$ ) for the fully extended blade.

### 5.1.3. Stresses in the Box Spar

Figure 5.7 shows the von Mises stress in each tension and compression zone in the box spar under the dead load. The horizontal axis presents the box spar length in meters, and the vertical axis shows the von Mises stress in each box spar section. The highest value of von Mises stress occurs at the largest width of the airfoil cross-sectional in the x-direction for each surface as shown. The differences between the two graphs are because of the loading that that exists on the tension surface of the box spar. Figure 5.8 presents the deflection and von Mises contours for the box spar. Because of the pressure is applied to the y-direction (the tension surface) of the skin. There are about 12% differences between the stresses on the two surfaces.

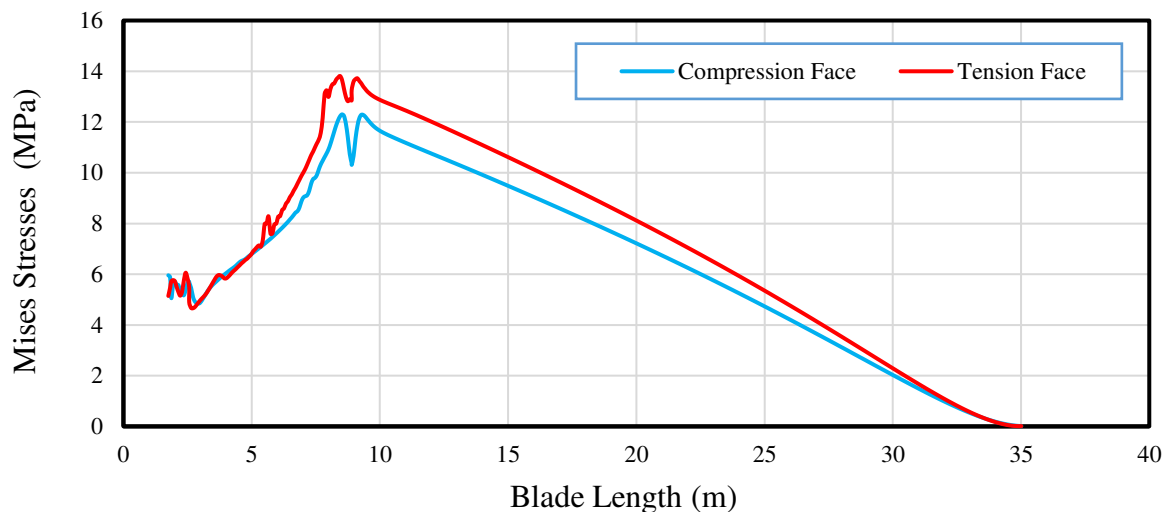


Figure 5.7: The von Mises stress on the tensile and compressive faces of the box spar.



Figure 5.8: The deflection and von Mises contours for the box spar.

Figure 5.9, and 5.10 show the tensile and compressive stresses acting on the box spar surfaces. As shown, each of the maximum tension and compression stress takes place at the largest width of the airfoil cross-sectional in the x-direction. The vertical axis presents the tension and compression stresses in MPa, and the horizontal axis presents the box length in meters. Also, Figure 5.11 shows the tension and the compression stress shapes for the box.

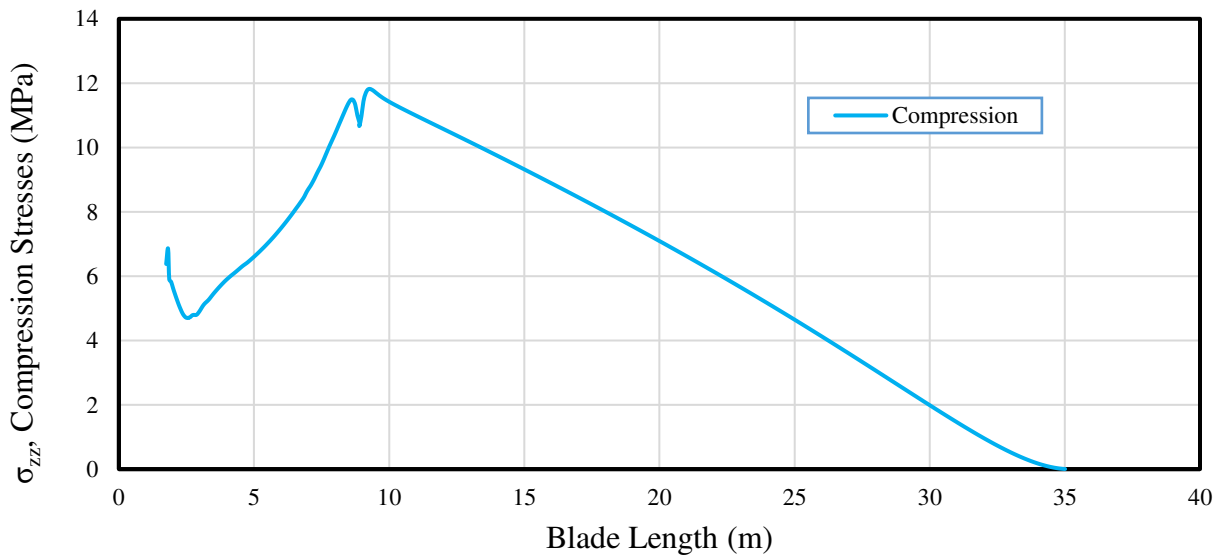


Figure 5.9: Compressive stresses in the z-direction for the box spar surface.

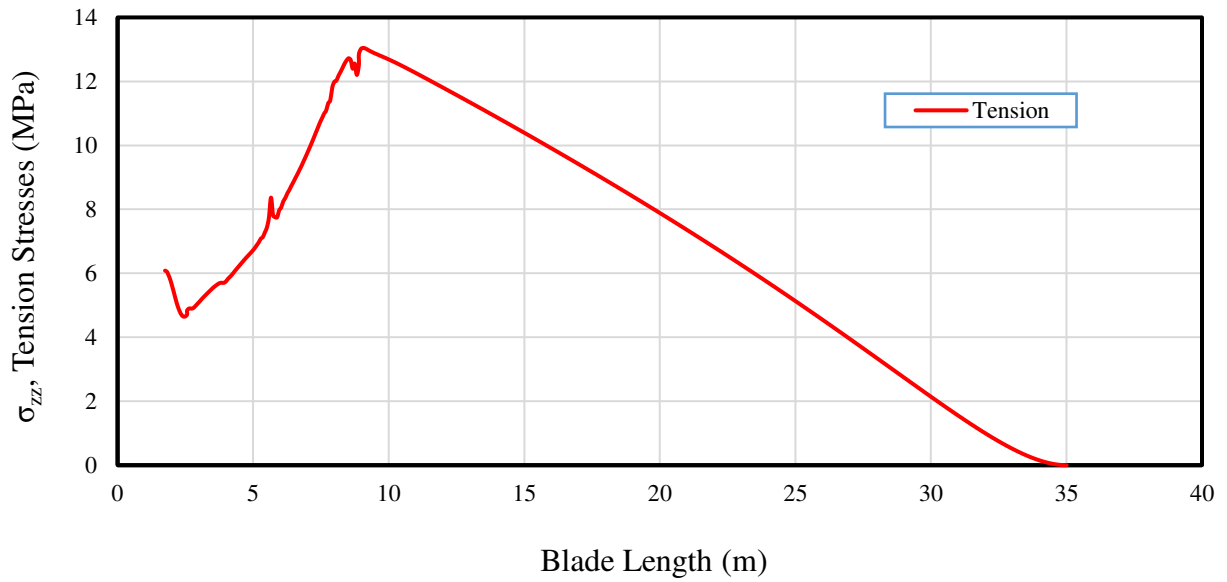


Figure 5.10: Tensile stresses in the z-direction for the box spar surface.

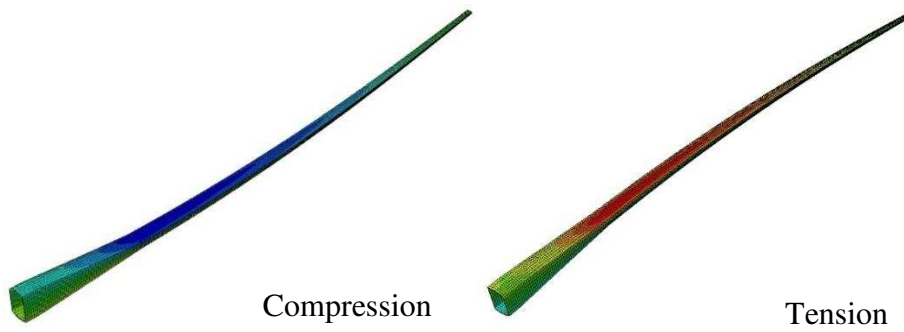


Figure 5.11: Stresses contours for ( $\sigma_{zz}$ ) for the full box spar.

## 5.2. Live plus Dead Load Case (Wind + Gravity)

### 5.2.1. Static Deflection for the Blade

Figure 5.12 presents the static deflection for the skin length under the pressure of the wind load and the skin weight. The horizontal axis shows the skin length in meters, and the vertical axis presents the deflection differences at each meter length. Figure 5.13 shows the deflection and von Mises stress contours for the conventional blade.

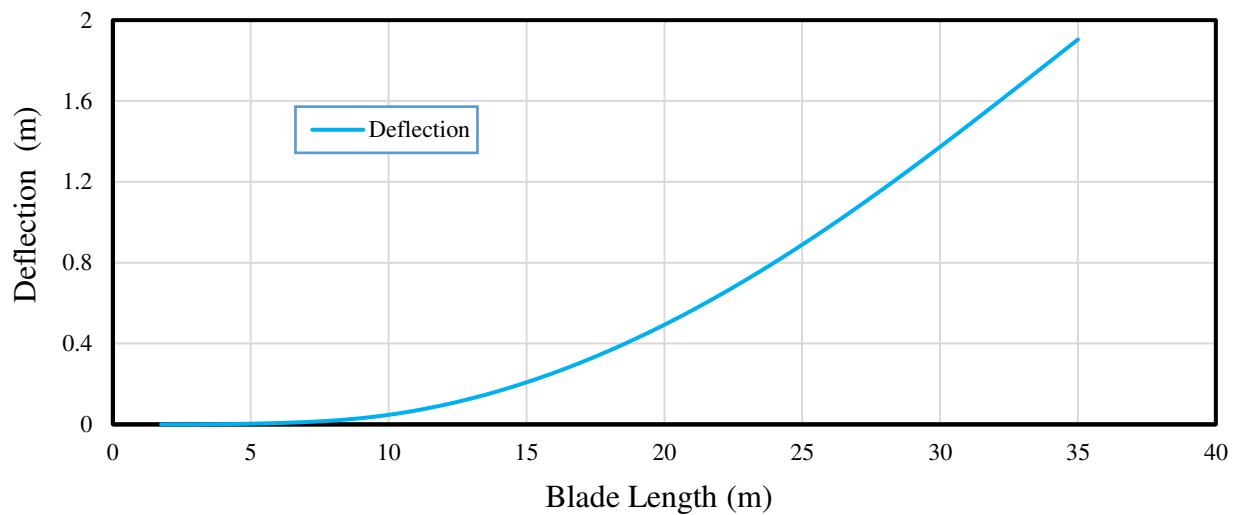


Figure 5.12: Static deflection for the fully extended blade.

### 5.2.2. Stresses at the Skin

The von Mises stress is shown in the Figure 5.13 for each tension and compression face under the pressure of the wind load and the skin weight. The horizontal axis presents the skin length in meters, and the vertical axis shows the von Mises stress in each skin sections. The highest value of von Mises stress is taking place at the largest width of the airfoil cross-sectional in the x-direction for each surface as shown in Figure 5.13. There is a 6% difference because of the placement of the load.

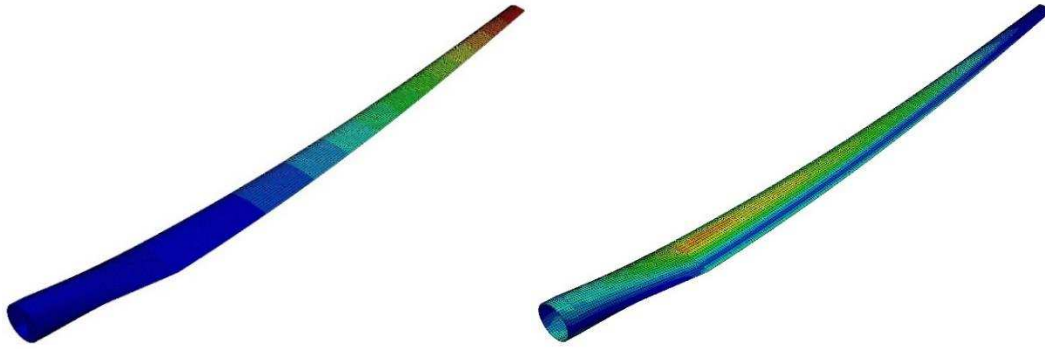


Figure 5.13: The deflection and von Mises stress contour for the conventional blade.

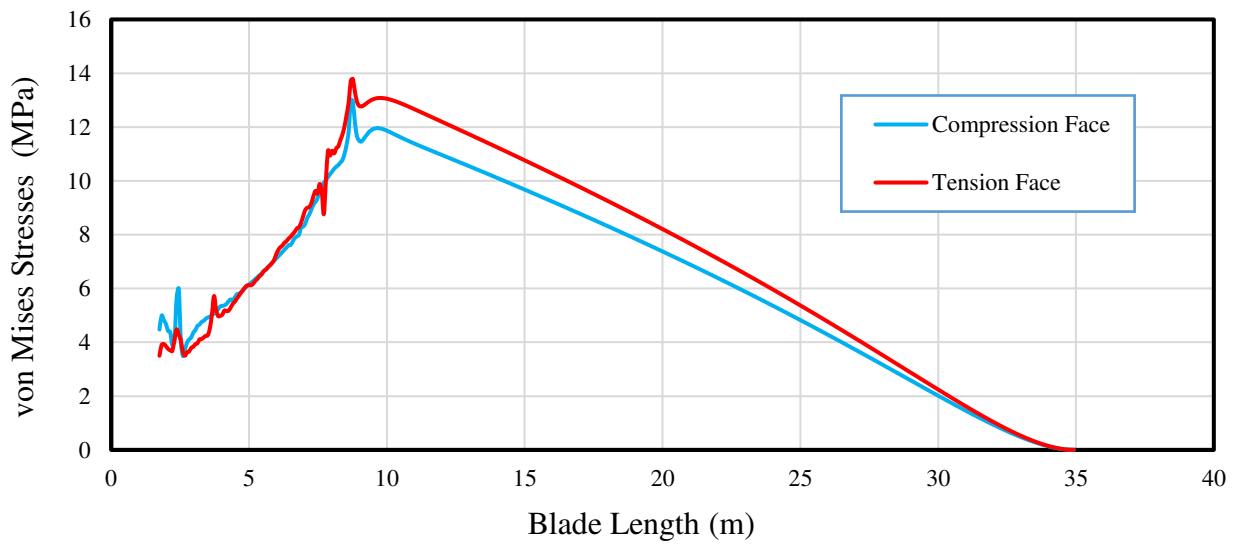


Figure 5.14: The differences of the von Mises stress in two surfaces for the fully extended blade.

Figures 5.15, and 5.16 show each of the tension and compression stresses acting on the skin under the pressure of the wind load and the skin weight. As shown, each of the maximum tension and compression stress is taking place at the largest width of the airfoil cross-sectional in the x-direction. The vertical axis presents the tension and compression stress in MPa, and the horizontal axis shows the skin length in meters. Also, Figure 5.17 presents the tension and the compression stress contour for the skin.

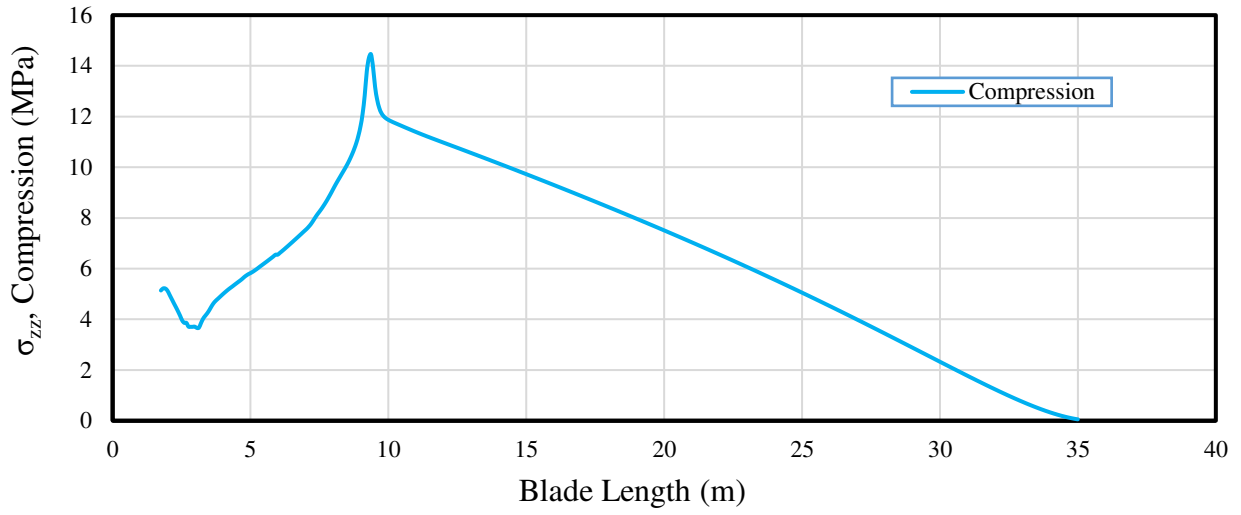


Figure 5.15: Compressive bending stresses in the z-direction.

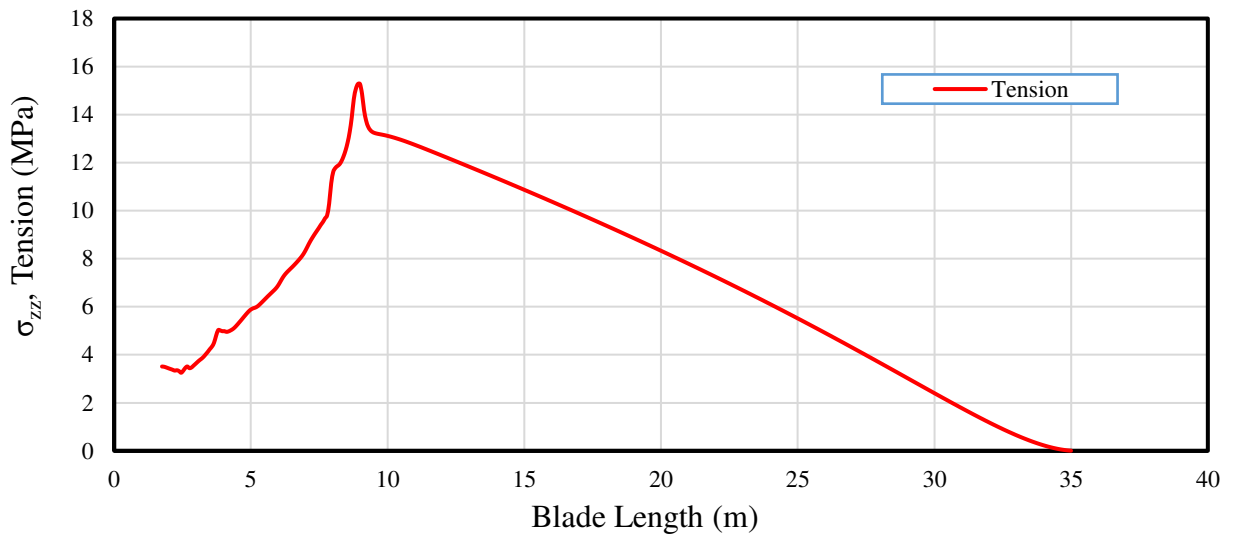


Figure 5.16: Tensile bending stresses in the z-direction.

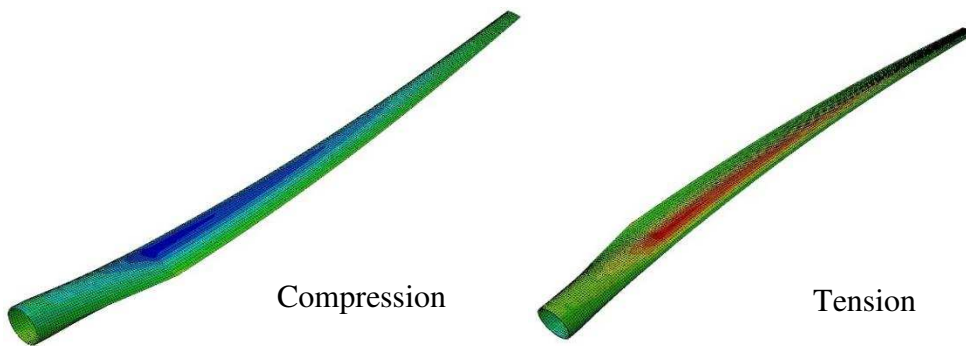


Figure 5.17: The stresses contours for ( $\sigma_{zz}$ ) for the fully extended blade.

### 5.2.3. Stresses in the Box

Figure 5.18 shows the von Mises stress in the tension and compression surfaces under the wind load and the box weight. The horizontal axis presents the box length in meter, and the vertical axis presents the von Mises stress in each box sections in MPa. The maximum von Mises stress at the highest width of the airfoil cross-section in the x-direction for each surface. There is an 11% difference between the two graphs because of the loading surface. Figure 5.19 shows the deflection and von Mises stress contour for the box spar.

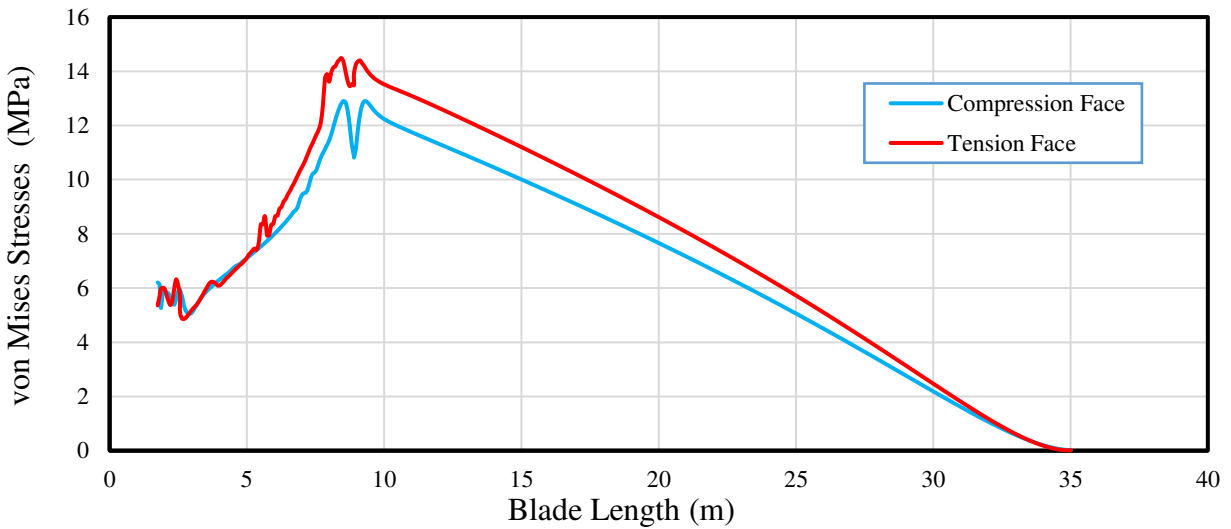


Figure 5.18: The differences of the von Mises stress in two surfaces for box spar.



Figure 5.19: The deflection and von Mises stress contour for the box spar.

Figure 5.20 and 5.21 show each of the tension and compression stress acting on all skin length under both the wind load and the box weight. As shown, each of the maximum tension and compression stresses is taking place in both figures at the largest width of the airfoil cross-sectional on the x-direction. The vertical axis presents the tension and compression stress in MPa, and the horizontal axis shows the box length in meters. Also, Figure 5.22 presents the tension and the compression stress contour for the box spar.

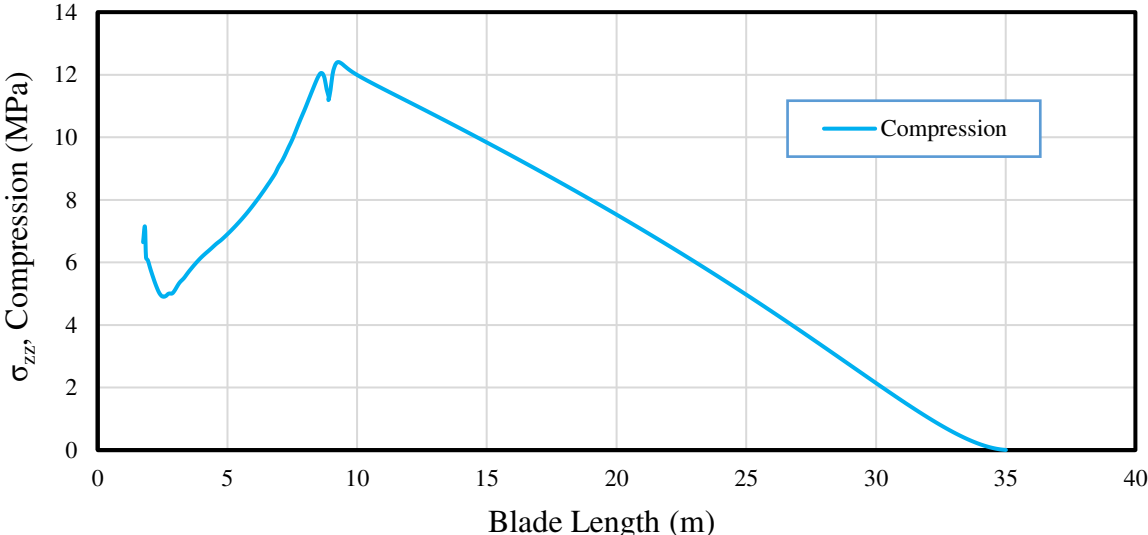


Figure 5.20: Compressive stresses in the z-direction.

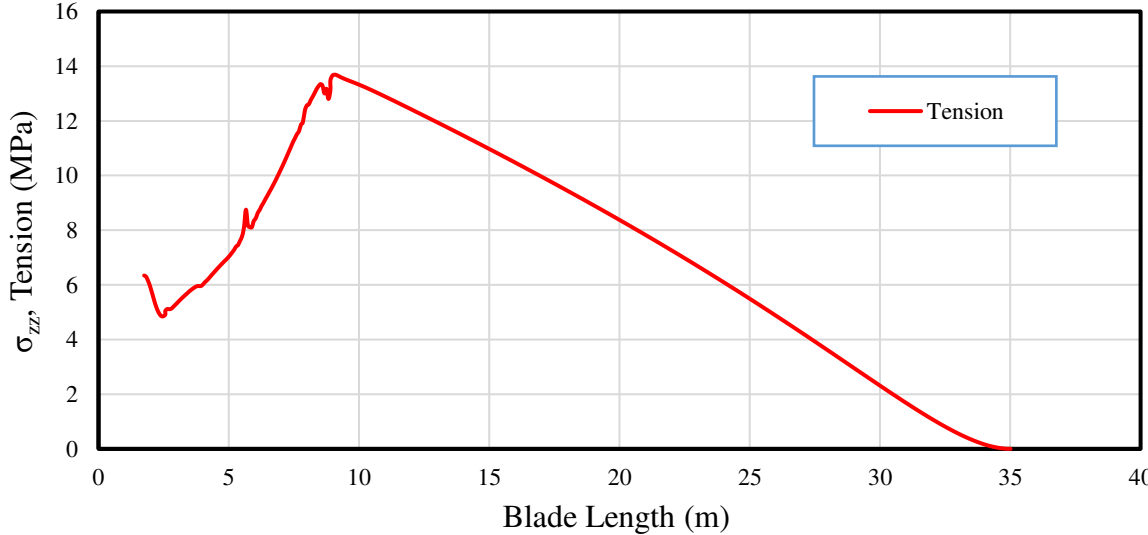


Figure 5.21: Tensile stresses in the z-direction.



Figure 5.22: Stresses contour for  $(\sigma_{zz})$  for the full box spar.

### 5.3. Stress as a Function of Position

#### 5.3.1. Fully Extended Blade

The stresses in the blade change as the angle the blade makes with the downward vertical position changes. In Figure 5.23, the von Mises stresses for the conventional blade while it is rotating under both of live load and dead load (the wind and gravity load) are shown. The vertical axis presents the von Mises stresses that affects the blade, and the horizontal axis presents the rotation angle for each 5-degree. The two graphs indicate each of the von Mises stresses for dead load and dead load with the live load. As shown, the maximum von Mises stresses occur at a 90-degree angle which is the horizontal position of the blade under both of load cases. The red graph presents the von Mises stresses under the two loads are applied, and the blue graph shows the stresses under just the gravity load. Both graphs are stayed the same and increased to the maximum value of von Mises stresses at 90-degree, horizontal position. Hence it appears that the bulk of the stresses are induced because of the dead load based on the blade weight.

Figure 5.24 shows the relationship between the blade rotation angles with the longitudinal stresses  $(\sigma_{zz})$  in the z-direction. The vertical axes present the longitudinal stresses  $(\sigma_{zz})$  that affect the blade, and the horizontal axes introduce the rotation angle for each 5-degree. The maximum longitudinal stresses  $(\sigma_{zz})$  at the horizontal position for the blade (90-degree) under wind load and

blade weight. Also, the chart includes both graphs, red presents the wind, and gravity loads are applied, and blue shows the gravity load only, of the longitudinal stresses ( $\sigma_{zz}$ ). There are slight differences between two graphs about 2%. For the principal stresses, the two graphs went up to the maximum value at the horizontal position. Also, Figure 5.25 presents the longitudinal stresses ( $\sigma_{zz}$ ) contour while the blade is rotated comparing the wind pressure only with wind and blade weight for each of  $0^\circ$ ,  $90^\circ$ , and  $180^\circ$ .

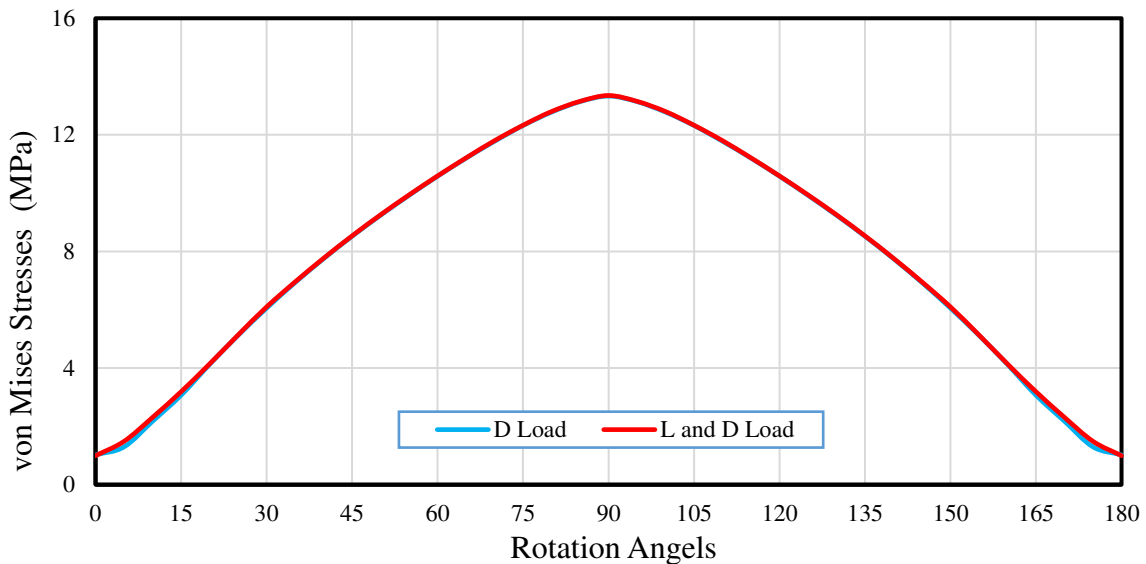


Figure 5.23: The von Mises stress while the blade rotation.

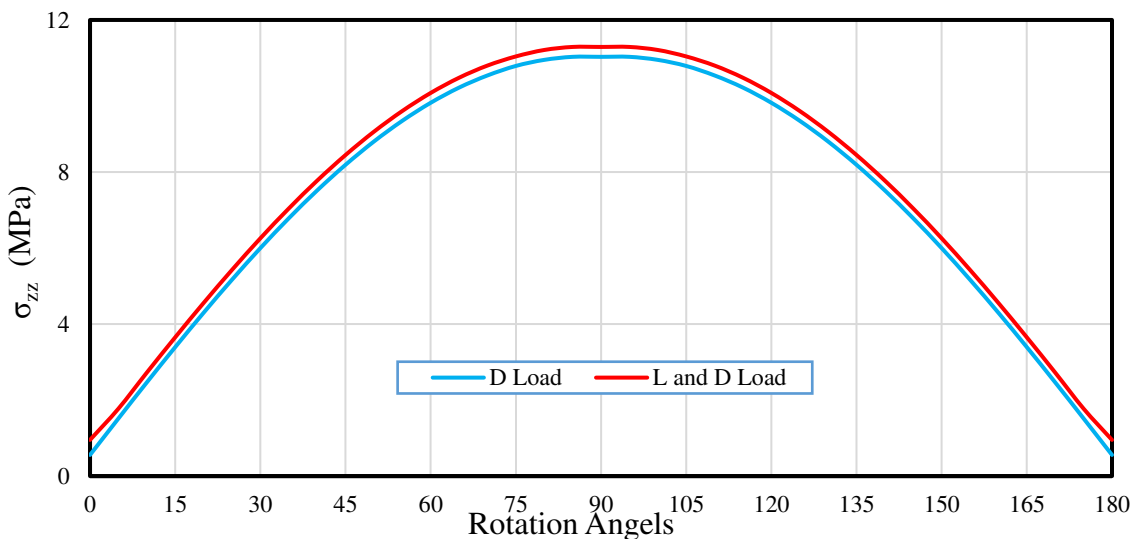


Figure 5.24: The principle stresses ( $\sigma_{zz}$ ) in z-direction while the blade rotation.

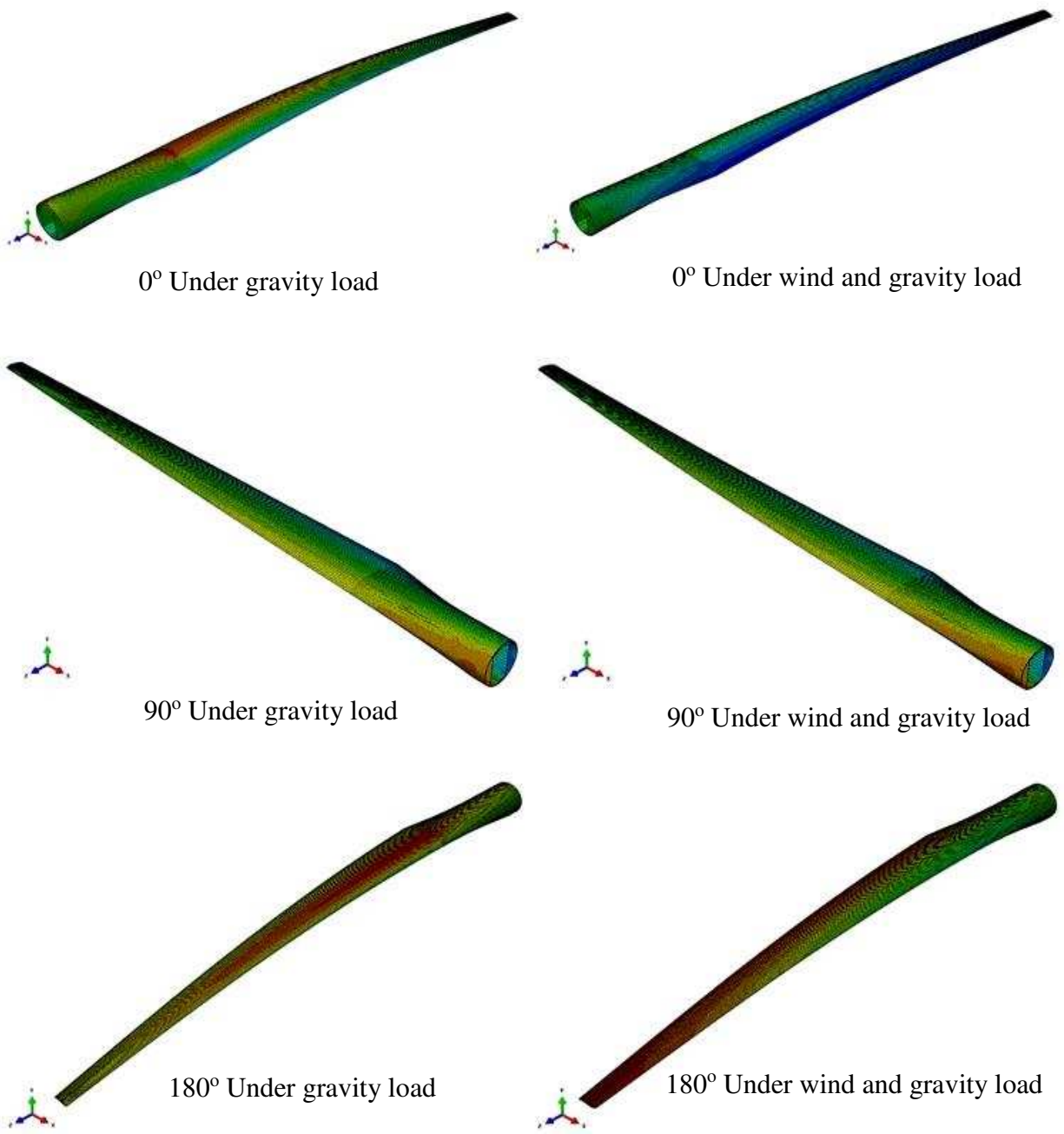


Figure 5.25: Stresses ( $\sigma_{zz}$ ) contour while the blade rotated at 0°, 90°, and 180°. The position of the blade is changed for viewing purposes.

### 5.3.2. The Folded Blade

When the blade is folded, the displacement and stress fields change significantly. In this section, the same loading conditions are used as for the conventional blade, with particular attention paid to the difference induced by the new geometry. Figure 5.26 presents the von Mises stresses while the folded blade is rotating under gravity load and the wind pressure with gravity load. The two charts in Figure 5.26 and 5.27 indicate each of the von Mises stresses and longitudinal stresses comparing between gravity load only and the wind with gravity load. The vertical axis presents the von Mises stresses that affects the folded blade, and the horizontal axis presents the rotation angle for each 5-degree. As with the case of the conventional blade, the maximum von Mises stresses value at 90-degree angle which is the horizontal position of the folded blade under both of load cases. The red graph shows the von Mises stresses under wind load with the folded blade weight, while the blue graph shows the stresses under only blade weight. There are about 5% differences between the two graphs.

Figure 5.27 presents the relationship between the folded blade rotation angles with the longitudinal stresses ( $\sigma_{zz}$ ) in the z-direction. Also, the maximum longitudinal stresses ( $\sigma_{zz}$ ) at the horizontal position for the blade (90-degree) under both of load cases. Also, the chart includes both graphs, the red graph shows the stresses under the wind with gravity load, and the blue graph shows the stresses under gravity load only, of the longitudinal stresses ( $\sigma_{zz}$ ). The vertical axis presents the longitudinal stresses ( $\sigma_{zz}$ ) that affect the blade, and the horizontal axis shows the rotation angle for each 5-degree. The graphs increased slightly and remained constant between of them and reached the maximum value at the horizontal position. Also, Figure 5.28 shows the comparison in von Mises stresses between the conventional blade and the folded blade at the folding edge while both blades are rotating at 0°, 90°, and 180° angles under both cases of loading.

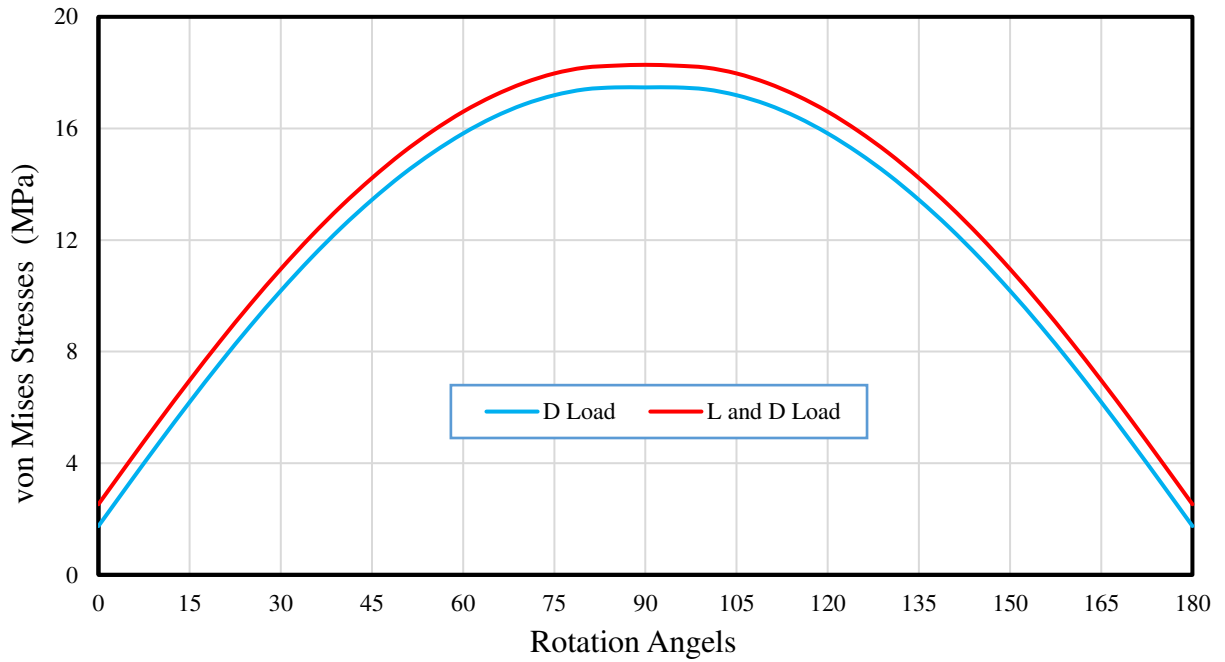


Figure 5.26: The von Mises stresses while the blade rotation.

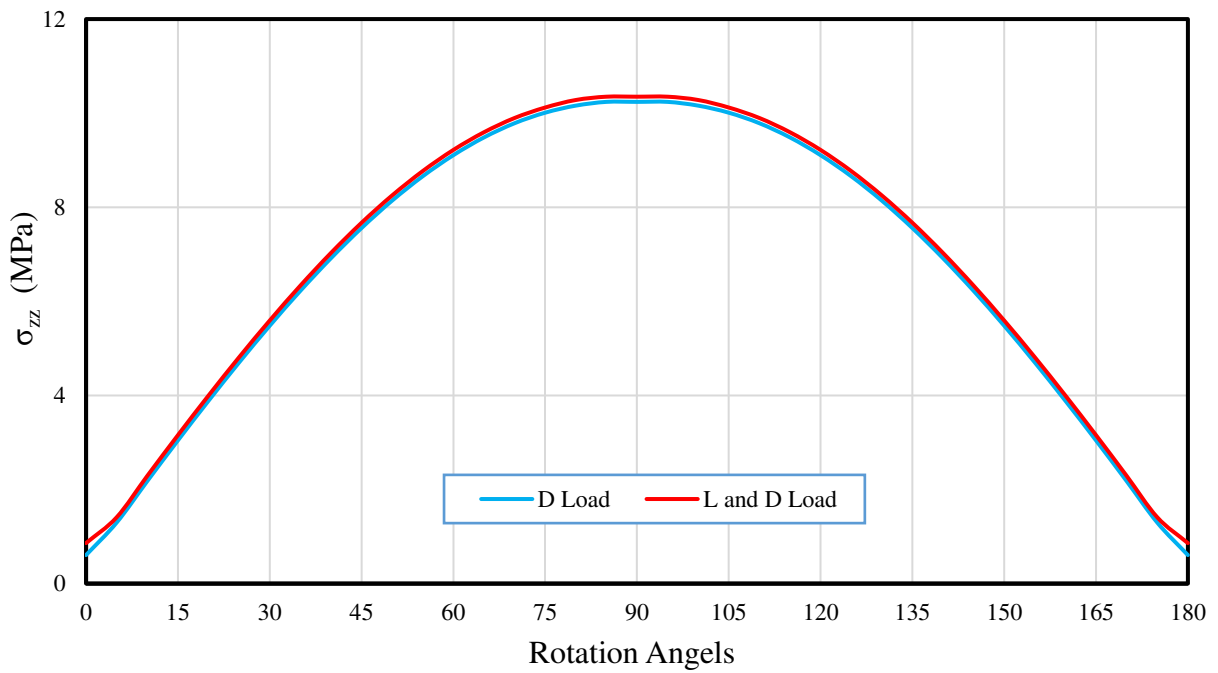
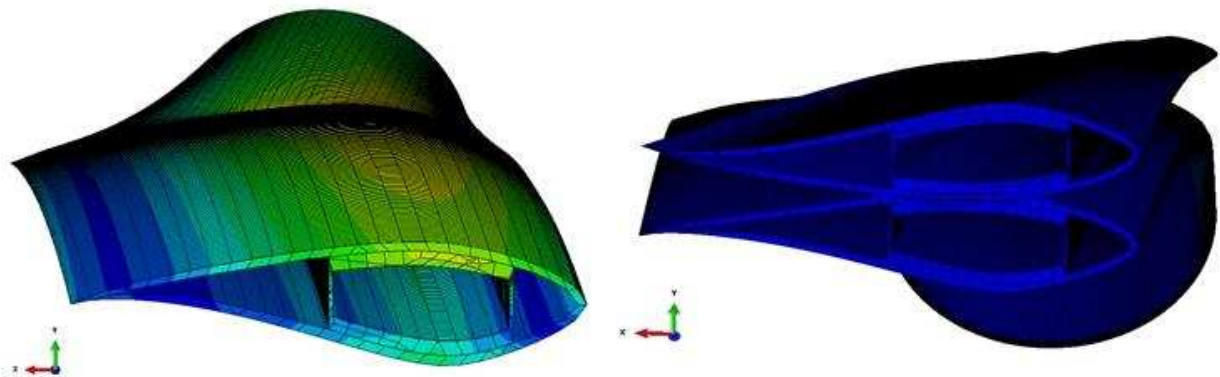
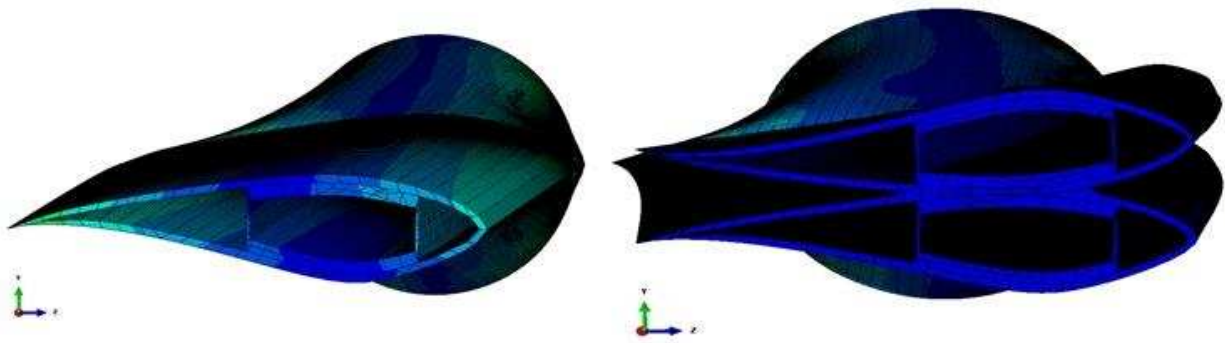


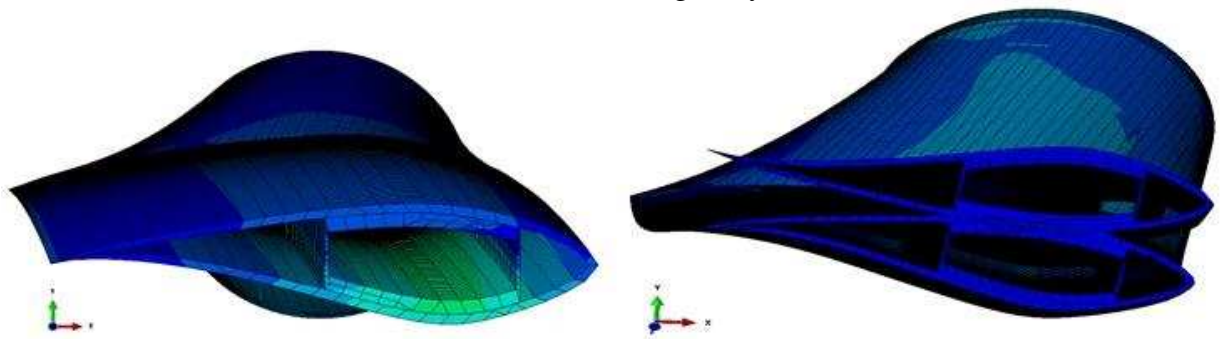
Figure 5.27: The principle stresses ( $\sigma_{zz}$ ) in z-direction while the blade rotation.



0° Under wind and gravity load



90° Under wind and gravity load



180° Under wind and gravity load

Figure 5.28: The comparison in von Mises stresses between conventional and folded blade.

#### 5.4. Folded Blade Stresses at The Cutting Edges:

Figures 5.29, 5.30, and 5.31 present each of von Mises stresses and longitudinal stresses on x-direction at the cutting edges of the folded blade under the gravity load only. The horizontal axis shows the cutting edges length in meters, and the vertical axis presents the von Mises stresses and stresses on x-direction in each chart in MPa. The maximum stresses value at the combined length of the cutting edges of each graph. Figure 5.29 has two graphs that present the von Mises stresses for the cutting edges; the red graph shows the bottom edge and the blue present the top edge. Figures 5.29 and 5.30 shows each of the tension and the compression stresses respectively at the connected edges. As shown, both charts indicate the maximum value of the stresses at the middle of the connections because of the box spar columns resist the weight of the skin.

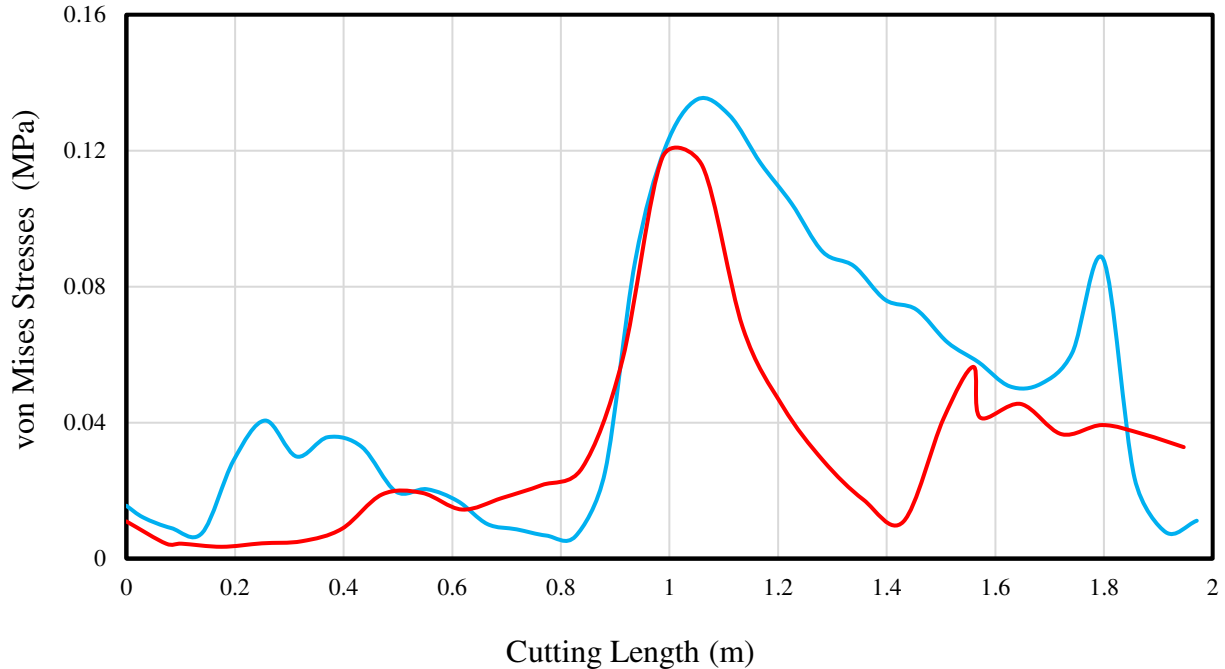


Figure 5.29: The Differences of the von Mises Stresses.

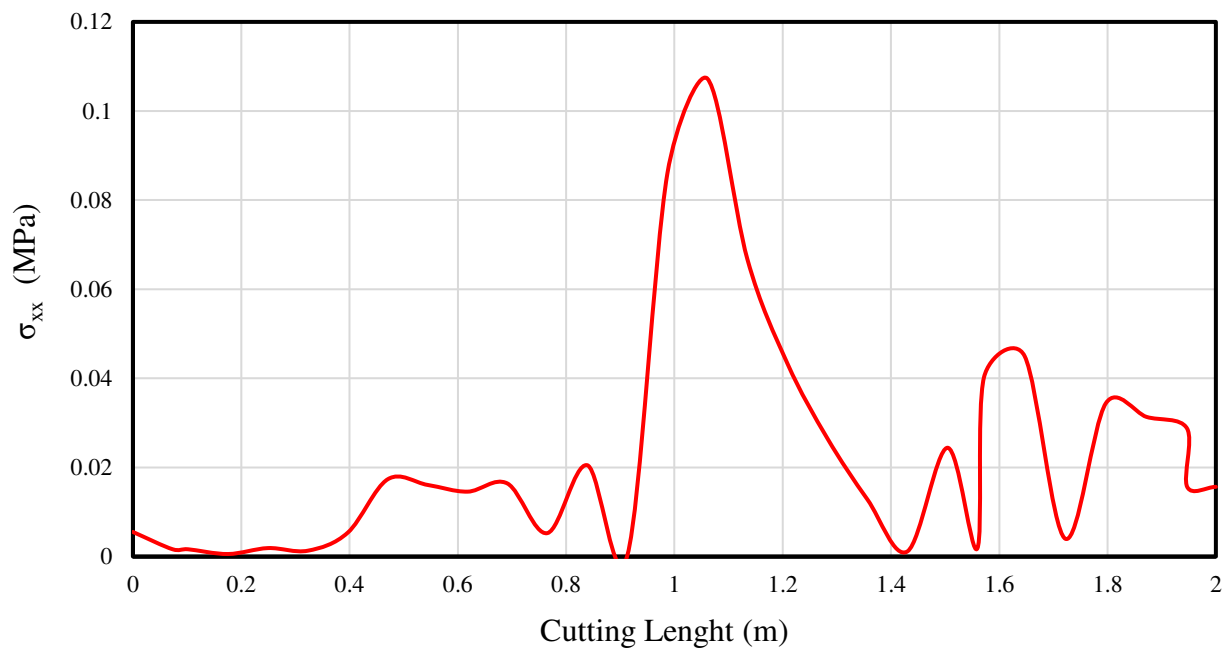


Figure 5.30: Tensile stresses in the x-direction.

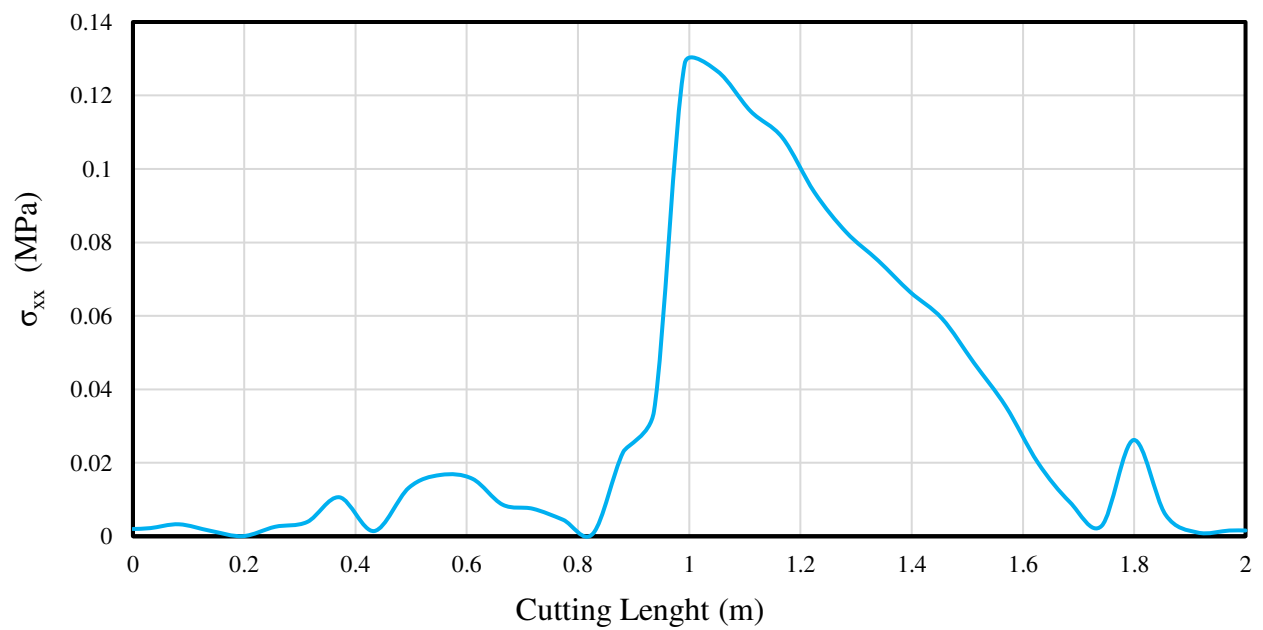


Figure 5.31: Compressive stresses in the x-direction.

## 5.5. Fundamental Frequency of Vibration

This section presents all the results for vibration analysis for both the conventional and folded blades. The two tables below show the result of the all vibrational modes and frequencies for both fully extended and folded blades.

### 5.5.1. Vibrational Mode and Frequency of Blade

Table 5.1 and 5.2 show the vibrational mode and the frequencies for the both types of the blades.

Figures 5.32 and 5.33 show all the vibration modes for both of conventional and folded blade respectively

Table 5.1: Vibrational Modes and Frequencies of Conventional Blades.

Number of Modes		Vibration Frequencies (Hz)
1	Flapwise	0.53016
2	Edgewise	1.2254
3	Flapwise	1.7847
4	Edgewise	3.9995
5	Flapwise	4.0124
6	Flapwise	7.1226
7	Edgewise	9.0488
8	Flapwise	11.010
9	Flapwise	15.569
10	<b>Torsion</b>	16.266

Table 5.2: Vibrational Modes and Frequencies of Folded Blades.

Number of Modes		Vibration Frequencies (Hz)
1	Flapwise	1.1608
2	Edgewise	1.9921
3	Flapwise	6.1449
4	Edgewise	9.8617
5	Flapwise	10.069
6	Flapwise	12.134
7	Edgewise	13.69
8	Flapwise	15.196
9	Flapwise	15.535
10	<b>Torsion</b>	15.788

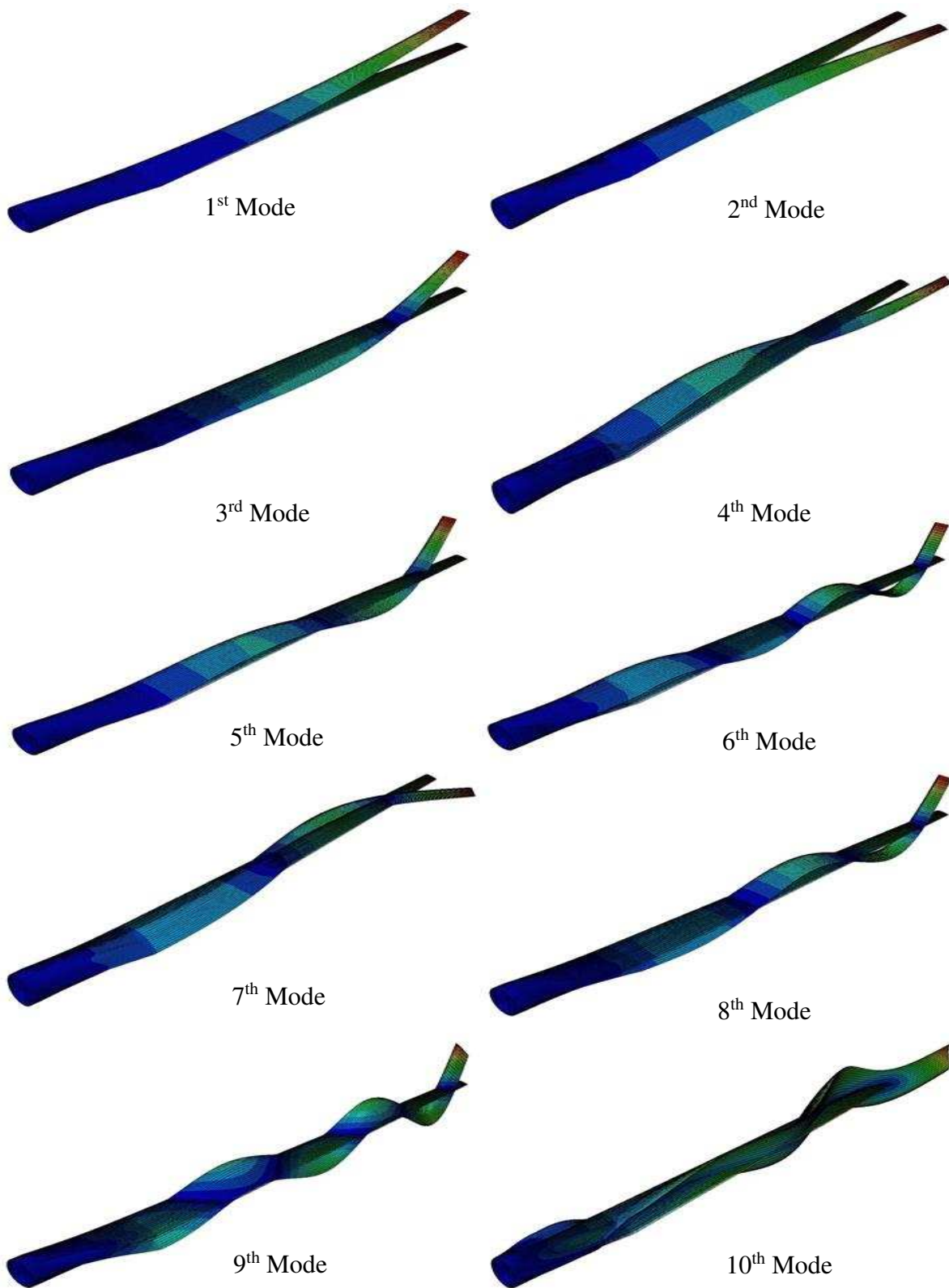


Figure 5.32: All vibration modes contour for the fully extended blade.

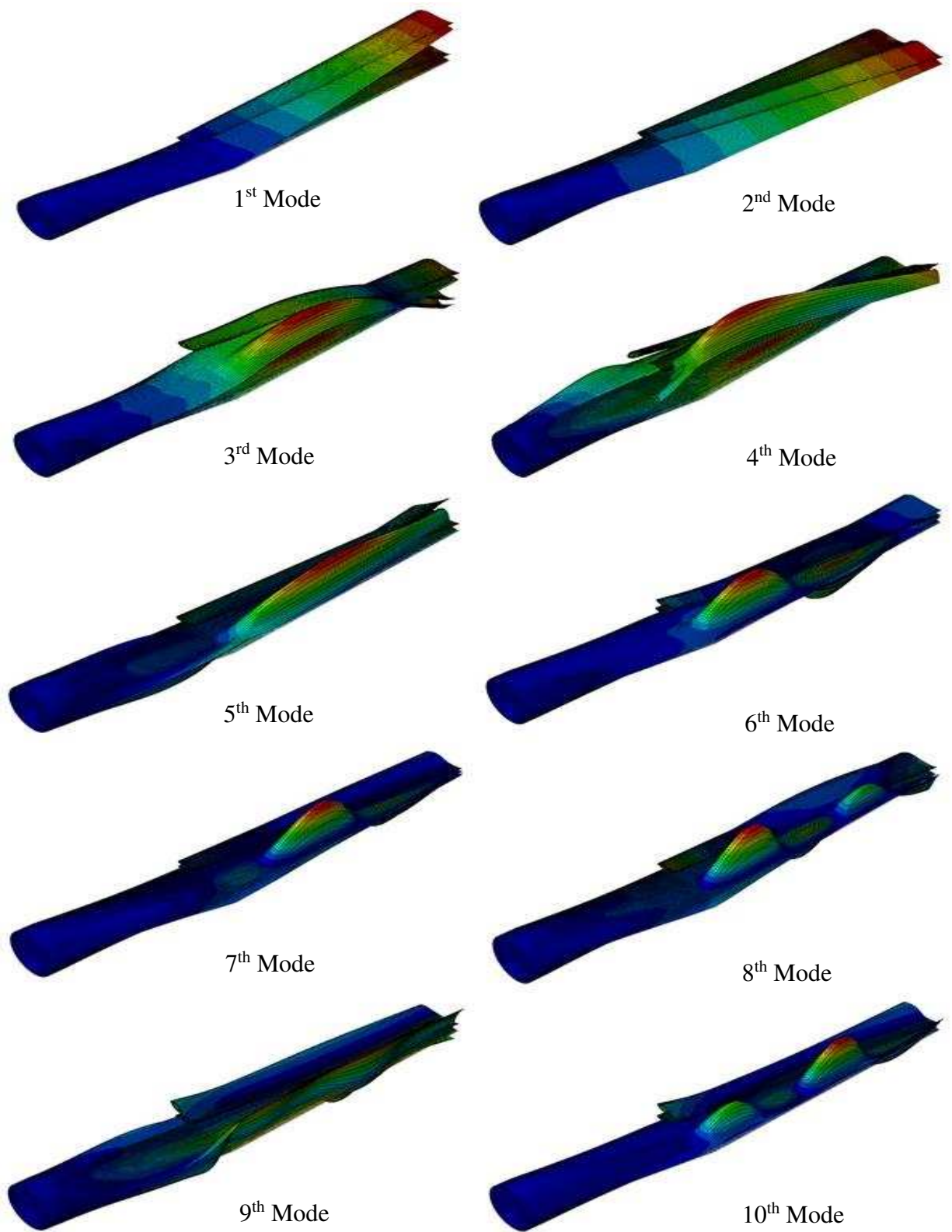


Figure 5.33: All vibration mode contour for the folded blade.

## DISCUSSION

### 6.1. Static Deflection:

Chapter 5 presents all the deflection results for the conventional blade under all load cases. Figure 6.1 presents the comparison of maximum deflection under both dead load only and wind load with gravity load. As it showed, there are small differences between the two load cases. Due to the significant length of the blade (33.25 meters), the deflection differences are 0.1 meters which are the wind load effects on the blade deflection by 5%. The vertical axis presents the load cases, and the horizontal axis shows the maximum deflection values in meters.

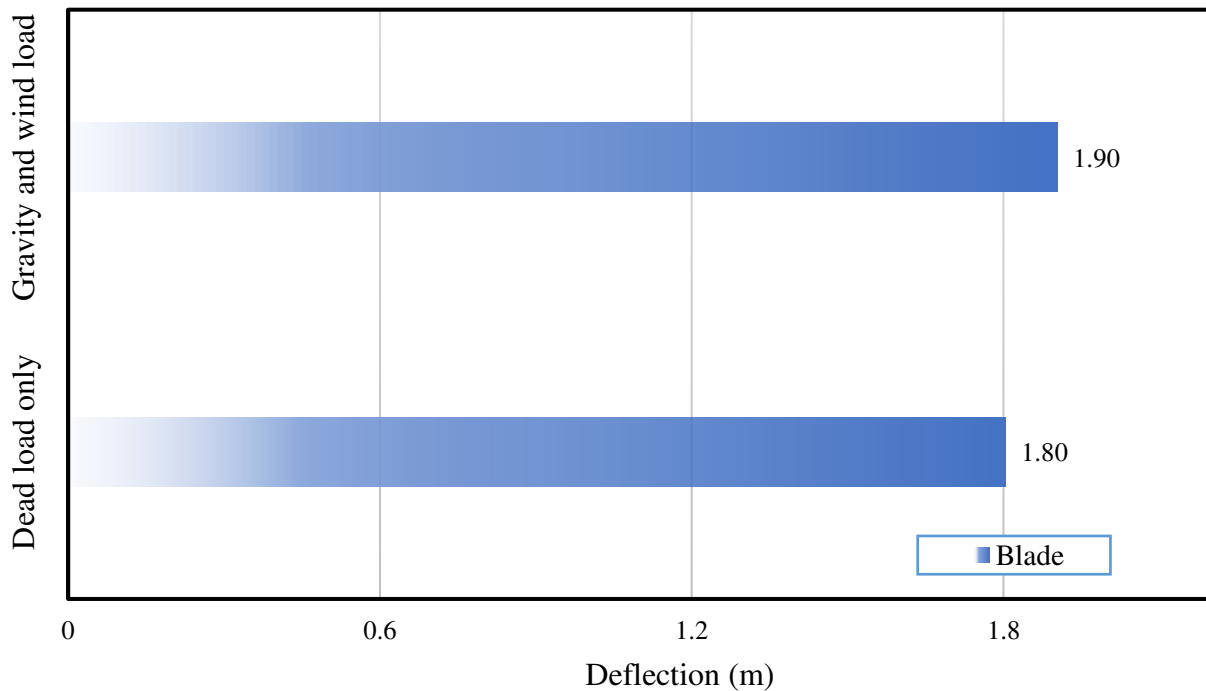


Figure 6.1: The comparison between blade's deflections.

## 6.2. Stresses:

As mentioned before, all the stresses results were computed using ABAQUS CAE. Figures 6.2 to 6.5 show all the comparison on stresses (von Mises stresses and stresses in the z-direction  $\sigma_{zz}$ ) for the fully extended blade (skin and box spar). The horizontal axes present the stresses values for von Mises and ( $\sigma_{zz}$ ) stresses, and the vertical axes present the two load cases. Figure 6.2 has a slight difference in von Mises stress for the skin between the two surfaces under the dead load only with approximately 5% as well as the other load case which is 6%. Also, von Mises stress for the box, Figure 6.3, has differences of 10% under both load cases.

For Figures 6.4 and 6.5, the principal stresses for the skin and box spar ( $\sigma_{zz}$ ) show the comparisons in stresses for all in the tension and compression under gravity and wind with gravity load case. There are about 5% differences in the stresses for both of load cases for Figure 6.4. Also, in Figure 6.5 the differences in stresses for each load case are about 10%.

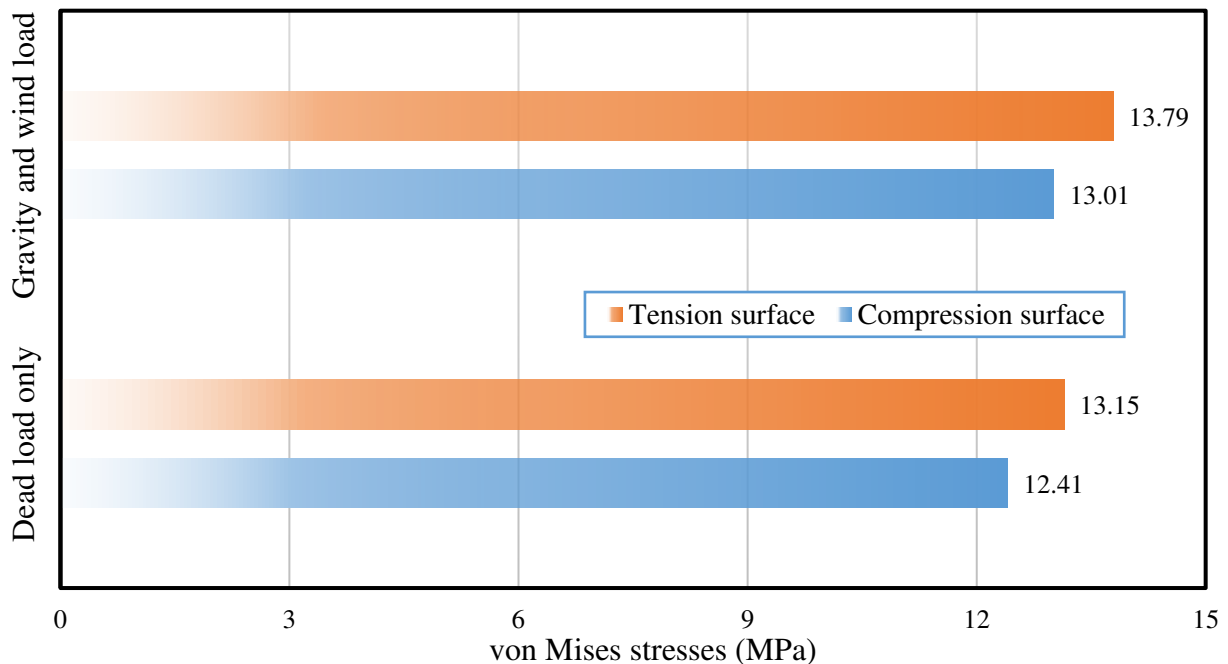


Figure 6.2: The comparison between von Mises stresses for the skin only.

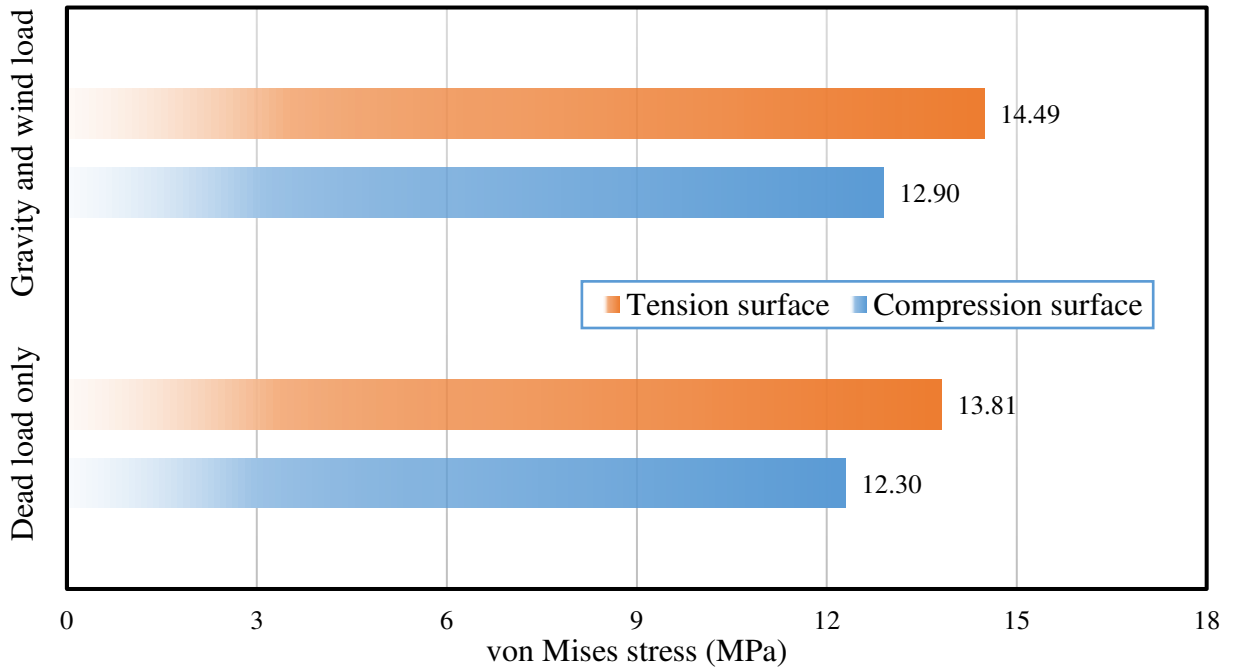


Figure 6.3: The comparison between von Mises stresses for the box spar only.

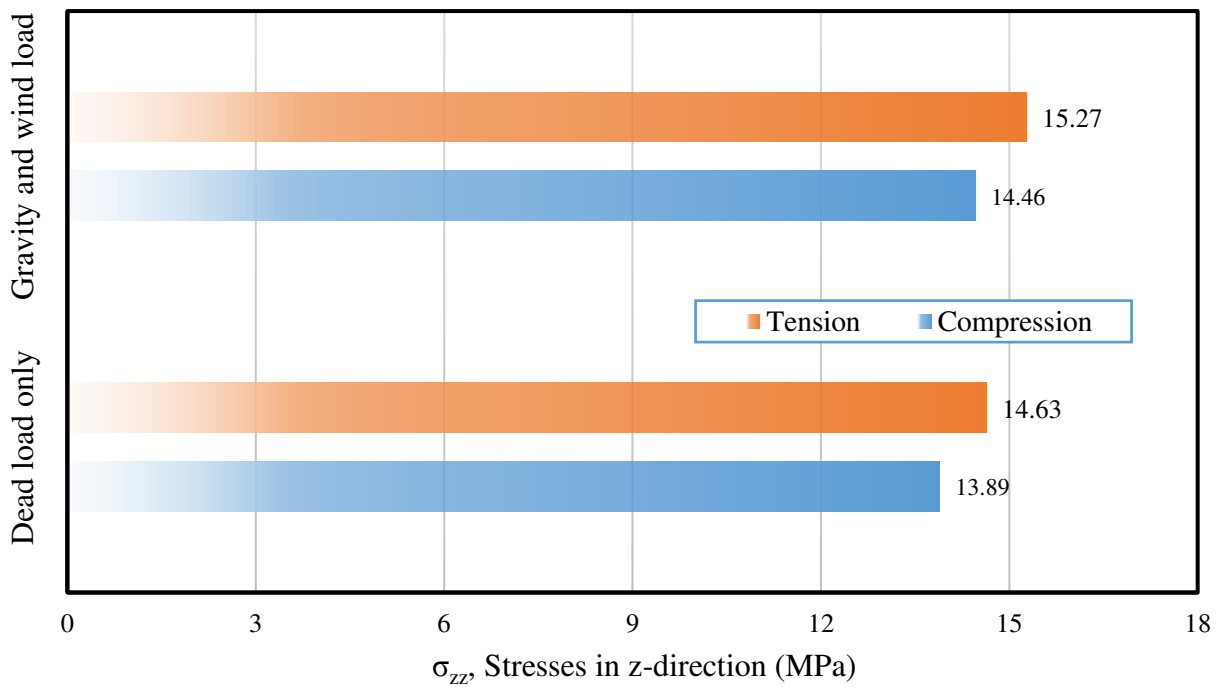


Figure 6.4: The comparison between stresses ( $\sigma_{zz}$ ) for the skin only.

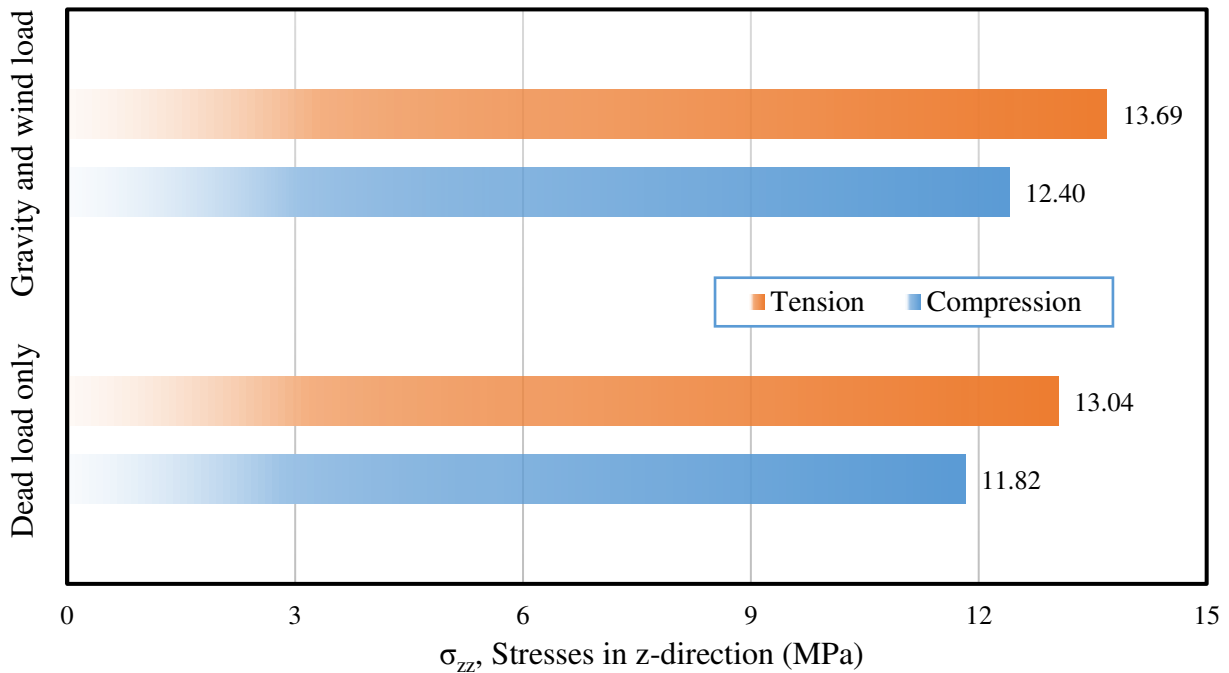


Figure 6.5: The comparison between stresses ( $\sigma_{zz}$ ) for the box spar only.

Under the load cases, wind load only and gravity and wind load, stresses are slightly similar in value for conventional and folded blades while the blades are rotating between the two charts. Figure 6.5, and 6.6 present the maximum ( $\sigma_{zz}$ ) and von Mises stresses for the fully extended and folded blades. The maximum stresses occurred close to the blades' root while both blades reached the 90-degree angle. At this position 90-degree, the blades act as a cantilever beam, and the weight of the blade and the wind load distributed on all blade's length in the transverse direction that affects more at the root of the blades. The weight of the Blade and wind loads cause differences of the stresses more than the gravity load only because wind load helps the blade rotating and effects on the tension surface of the blade while the maximum stresses take place on the root that holds the blades.

It can be clearly noticed that the differences in von Mises stress are about 24% between of folded and fully extended blade as shown in Figure 6.6, also about the same percentage which is 27% of differences for von Mises stress Figure 6.7. Principle stresses ( $\sigma_{zz}$ ) for both charts, Figures 6.6 and 6.7, show that about 8% and 10% differences respectively.

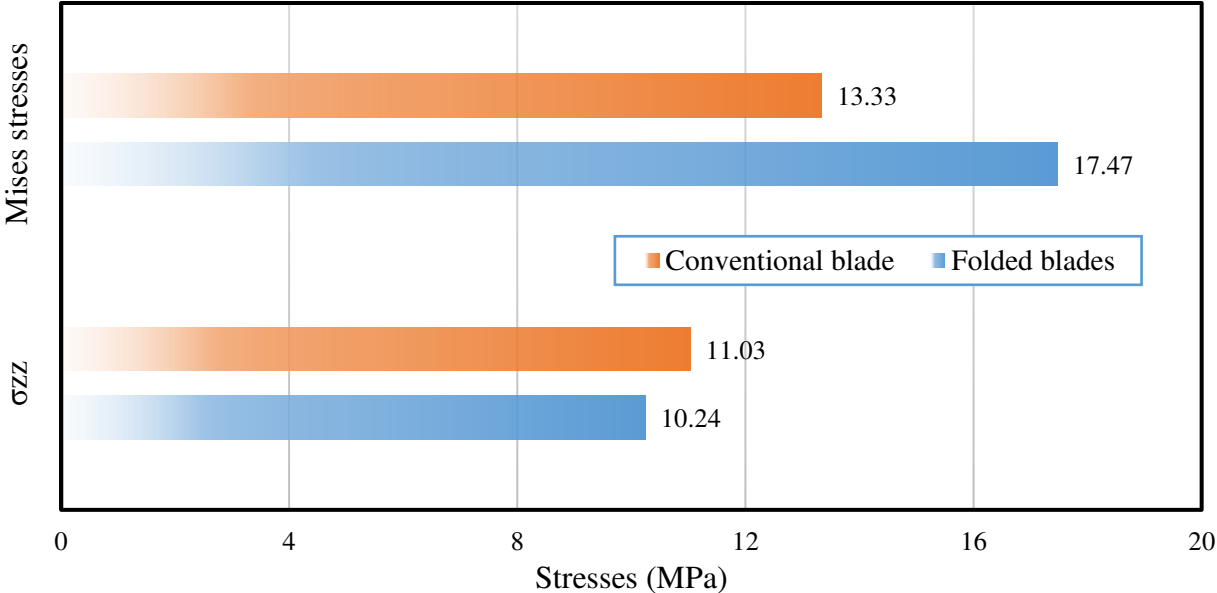


Figure 6.6: Comparing between folded and fully extended blades stresses under gravity load.

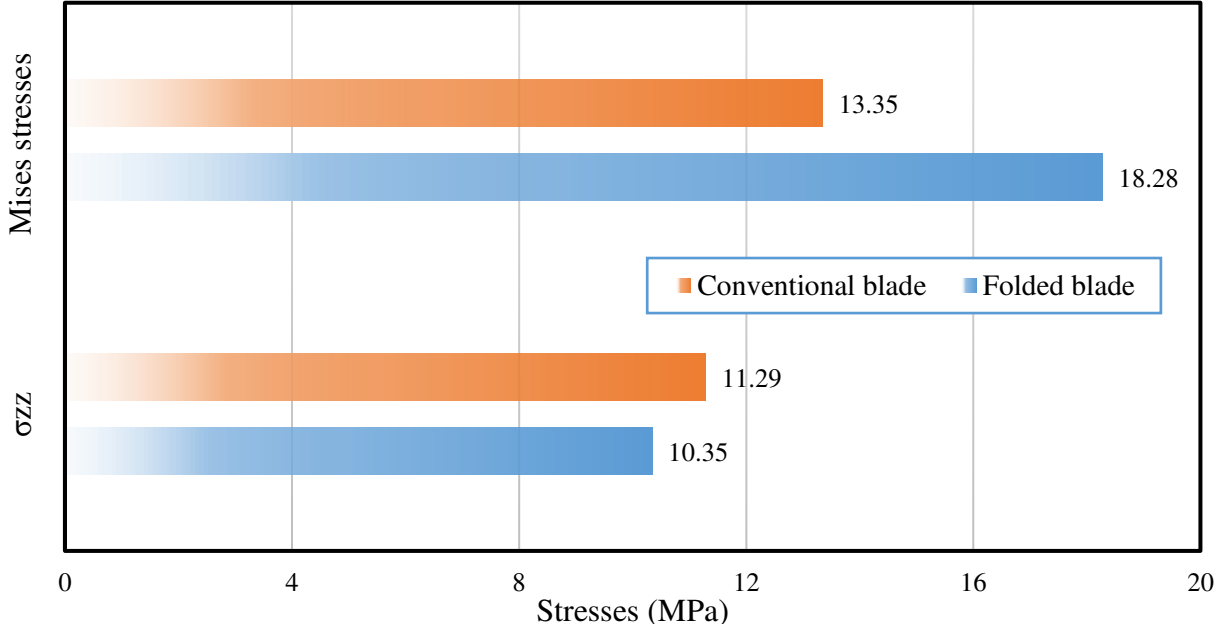


Figure 6.7: Comparing between folded and fully extended blades stresses under all load cases.

Figure 6.8 shows the maximum longitudinal ( $\sigma_{xx}$ ) in the x-direction, and von Mises stresses at the attached edges of the folded blade. The vertical axis presents both types of the stresses that affect the top and the bottom edges, and the horizontal axis presents the maximum stresses values. As shown, all edges have almost an equal value of stresses, but the maximum stresses occurred on bottom edge due to the folding part weights, and the differences are 14% for the both cases of stresses.

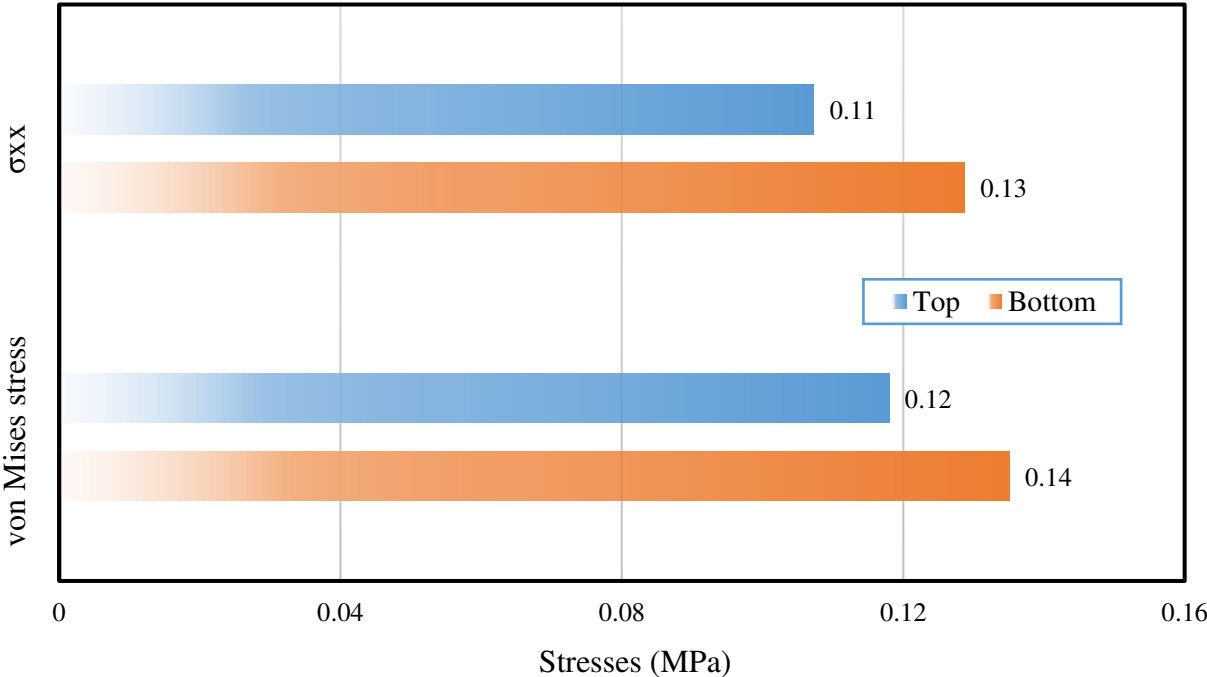


Figure 6.8: Transverse ( $\sigma_{xx}$ ) and von Mises stresses on folded blade edges.

## CONCLUSIONS

The Stresses and frequency shifts in fully extended and folded wind turbine blades were proposed. Both the fully extended and the folded blade was designed and analyzed. All the results consist the understanding of the changes in the displacements, stresses, and natural frequencies of fully extended and folded wind turbine blades. The following conclusions are obtained in current research:

1. The static deflection of the fully extended blade has more displacement under gravity with wind load more than wind load only.
2. Even though using von Mises stress as a yield strength for an isometric material, von Mises stress were used in the results to give an indication of how yield strength values could be as close for the yield strength values of the composite material (orthotropic material) that were used in the blades.
3. An 8.75 meters of the blade length, which is the largest airfoil width, provide maximum values of von Mises stresses and the longitudinal stresses in the z-direction ( $\sigma_{zz}$ ) for each case due to the change of the blade shape at this point under each of wind pressure only and gravity load with wind load.
4. For the folded blade, the both stresses (von Mises stresses and the longitudinal stresses in the x-direction ( $\sigma_{xx}$ )) on the connected edges are the maximum in the middle of the connected edges because of the resistance of spar box shear webs.

5. The fundamental vibrations frequencies for the folded blade are about two times more than the vibration frequencies for the conventional blade. However, for the torsion is almost similar to both the folded and the conventional blade.
6. The study illustrates the comparison on stresses (von Mises stresses and the longitudinal stresses ( $\sigma_{zz}$ ) for the fully extended blade and the folded blades under all load cases while the blades are rotating all the results taken at each of 5-degrees.

## REFERENCES

1. 10 Biggest Turbines in the world, from Wind Power Monthly,  
<http://www.windpowermonthly.com/10-biggest-turbines>.  
Revisited on 27 January 2014.
2. Beth Stackpole, Contributing Editor, Design Software & Hardware (January 2011) Sandia  
Sizes up Wind Turbine Blade Design. Retrieved from
3. Carl Sulzberger (2009). A bold effort in Vermont, *Power And Energy Magazine, Institute of  
Electrical And Electronics Engineers*, Vol.7, Issue 6, Pages 100-110.
4. Cesnik, C. E., & Hodges, D. H. (1997). VABS: A New Concept for Composite Rotor Blade  
Cross- Sectional Modeling. *Journal of the American helicopter society*, 42(1), 27-38.
5. Chen, H., Yu, W., & Capellaro, M. (2010). A critical assessment of computer tools for  
calculating composite wind turbine blade properties. *Wind Energy*, 13(6), 497-516.
6. Dayton A. Griffin (2002). Blade System Design Studies Volume I: Composite Technologies  
for Large Wind Turbine Blades, *SAND2002-1879. Albuquerque, NM: Sandia National  
Laboratories*.
7. Freight Management and Operations, Federal Highway Administration, U.S. Department of  
Transportation, from,  
[http://ops.fhwa.dot.gov/Freight/publications/size\\_regs\\_final\\_rpt/index.htm](http://ops.fhwa.dot.gov/Freight/publications/size_regs_final_rpt/index.htm).  
Revisited on 3 November 2014.
8. Gary L. Johnson, 1985. Wind Energy Systems, Illustrated, Prentice Hall PTR, London, 1985  
(Digitalized in July 2008)

9. GE Renewable Energy  
<https://www.gerenewableenergy.com/wind-energy/turbines/turbine-overview.html> Retrieved 6 November 2013.
10. History of Wind Energy, from Iowa Energy Centre <http://www.iowaenergycenter.org/wind-energy-manual/history-of-wind-energy/>.  
Revisited on 20 January 2014
11. Hodges, D. H., Shang, X., & Cesnik, C. E. (1996). Finite element solution of nonlinear intrinsic equations for curved composite beams. *American Helicopter Society, Journal*, 41(4), 313-321.
12. Imraan, M., Sharma, R. N., & Flay, R. G. (2009, January). Telescopic Wind Turbines to Capture Energy at Low Wind Speeds. In *ASME 2009 3rd International Conference on Energy Sustainability collocated with the Heat Transfer and InterPACK09 Conferences* (pp. 935-942). American Society of Mechanical Engineers.
13. Imraan, M., Sharma, R. N., & Flay, R. G. (2011, January). Wind Tunnel Testing of a Telescopic Blade Wind Turbine. In *ASME 2011 Power Conference collocated with JSME ICOPE 2011* (pp. 493-499). American Society of Mechanical Engineers.
14. John, J. (2015). *Mechanics of extendable wind turbine blades* (Doctoral dissertation, COLORADO STATE UNIVERSITY).
15. J. Jonkman, S. Butterfield, W. Musial, and G. Scott (February 2009). Definition of a 5MW Reference Wind Turbine for Offshore System Development, *National Renewable Energy Institute, NREL/TP-500-38060*. Revisited in June 2014.
16. J.W. Larsen, S.R.K. Nielsen (2006). Nonlinear parametric instability of wind turbine wings, *Journal of Sound and Vibration*, Vol 299, Issue 1-2, Pages 64-82.
17. Kane, T. R., & Levinson, D. A. (1985). *Dynamics, theory, and applications*. McGraw Hill.

18. Laird, D. L., Montoya, F. C., & Malcolm, D. J. (2005, January). Finite element modeling of wind turbine blades. In *43rd AIAA Aerospace Sciences Meeting and Exhibit* (Vol. 6, pp. 10-13).
19. Lee, D., Hodges, D. H., & Patil, M. J. (2002). Multi- flexible- body Dynamic Analysis of Horizontal Axis Wind Turbines. *Wind Energy*, 5(4), 281-300.
20. Malcolm, D. J., & Laird, D. L. (2007). Extraction of equivalent beam properties from blade models. *Wind Energy*, 10(2), 135-157.
21. Mechanical Properties of Carbon Fiber Composite Materials, Fiber / Epoxy resin (120°C Cure), <http://www.performancecomposites.com/about-composites-technical-info/122-designing-with-fiberglass.html>, Performance Composites Ltd., Revisited in February 2014.
22. Molenaar, D. P., & Dijkstra, S. (1999). State-of-the-art of wind turbine design codes: main features overview for a cost-effective generation. *Wind engineering*, 23(5), 295-312.
23. Pardo, D., & Branner, K. (2005). Finite element analysis of the cross-section of wind turbine blades; a comparison between the shell and 2D-solid models. *Wind Engineering*, 29(1), 25-32.
24. Patil, M. J., Hodges, D. H., & S. Cesnik, C. E. (2000). Nonlinear aeroelastic analysis of complete aircraft in subsonic flow. *Journal of Aircraft*, 37(5), 753-760.
25. Patrick. J. Moriarty, William E. Holley, Sandy Butterfield (2002). Effect Of Turbulence Variation On Extreme Loads Prediction For Wind Turbines, *American Society of Mechanical Engineers*, Vol. 124, Issue 4, Pages 387-395, November 2002.
26. Peters, D. A., Boyd, D. D., & He, C. J. (1989). Finite- State Induced- Flow Model for Rotors in Hover and Forward Flight. *Journal of the American Helicopter Society*, 34(4), 5-17.
27. Riziotis, V. A., Voutsinas, S. G., Politis, E. S., & Chaviaropoulos, P. K. (2004). Aeroelastic stability of wind turbines: the problem, the methods and the issues. *Wind Energy*, 7(4), 373-392.

28. Seanergy 2020: Final Project summary, May 2012.
29. Sørensen, P., Cutululis, N. A., Viguera- Rodríguez, A., Madsen, H., Pinson, P., Jensen, L. E., Hjerrild & Donovan, M. (2008). Modeling of power fluctuations from large offshore wind farms. *Wind Energy*, 11(1), 29-43.
30. Tartibu, L.K., Kilfoil, M. And Van Der Merwe, A.J (2012). Vibration Analysis Of A Variable Length Blade Wind Turbine, *International Journal of Advances in Engineering & Technology*, Vol 4, Issue 1, Pages 630-639, July 2012.
31. Technical Specs of Common Wind Turbine Models  
<http://www.aweo.org/windmodels.html>.
32. The Wind Energy Pioneers: The Gedser wind Turbine, Updated 23 July 2003, *Danish Wind Energy Association*,  
[http://www.motiva.fi/myllarin\\_tuulivoima/windpower%20web/en/pictures/juul.htm](http://www.motiva.fi/myllarin_tuulivoima/windpower%20web/en/pictures/juul.htm)  
Retrieved 3 February 2014.
33. Timeline: History of Wind Power, from The Guardian  
<http://www.theguardian.com/environment/2008/oct/17/wind-power-renewable-energy>.  
Revisited on 27 January 2014
34. Timothy J McCoy and Dayton A Griffin (2006). Active control of rotor aerodynamics and geometry: Status, methods, and preliminary results, *American Institute of Aeronautics and Astronautics Inc.*, In 44th AIAA/ASME.
35. Timothy J McCoy and Dayton A Griffin (2008). Control of rotor geometry and aerodynamics: Retractable Blades and Advanced Concepts, *Multi-Science Publishing Co. Ltd*, Vol. 32, Issue 1, Pages 13-26, January 2008.
36. Xie, W., Zeng, P., & Lei, L. (2015). A novel folding blade of wind turbine rotor for effective power control. *Energy Conversion and Management*, 101, 52-65.

37. Yu, W. (2007). Efficient High- Fidelity Simulation of Multibody Systems with Composite Dimensionally Reducible Components. *Journal of the American Helicopter Society*, 52(1), 49-57.